Master's Thesis

An Experimental Study of ^{8}B beta decay

Andreas Møsvraa Gaarde Gad

201303721

Supervisor: Karsten Riisager

Department of Physics and Astronomy
Aarhus University

June 2018

Abstract

This thesis presents a detailed analysis of the excitation spectrum of ^{8}Be, probed through β-delayed α-decay of ^{8}B. The analysis is based on data from the experiment IS633 conducted at the ISOLDE facility at CERN, Switzerland in May 2017.

The goal of this analysis is to determine the precise excitation spectrum of ^{8}Be. The primary focus is to measure the 2^+ doublet at 16 MeV, with more statistics than previously possible through β-decay of ^{8}B. More specifically, we are interested in the level at 16.922 MeV, which has only been measured once before with very limited statistics.

In order to achieve this, a careful calibration was made with corrections for energy-loss in different parts of the detector setup. The excitation spectrum was extracted based on coincidence measurements of the $\alpha - \alpha$ breakup of ^{8}Be, with an estimated precision of 11 keV at the doublet levels. The extracted spectrum has a factor of 93 more statistics than any previous experiment has achieved.

Lastly the spectrum was analyzed using R-matrix theory. In a comparison with the data from a previous experiment, it is shown that their model, results in a unphysical description of the 2^+ doublet levels. Four alternative models are investigated in a local fit to the 2^+ doublet, in an attempt to determine level parameters and the Gamow-Teller strength.

Outline

The thesis is divided into five chapters.

- Chapter 1 gives a motivation for the experiment, followed by an introduction to the subject and lastly, a brief discussion of previous measurements of the ^{8}Be spectrum.
- Chapter 2 describes the experimental methods. First, the radioactive beamline and detector setup is introduced, and some initial data analysis routines using the AUSAlib library are discussed. Then, various aspects of the detection system response are discussed, including calibrations and energy-loss corrections, followed by a discussion on the obtained energy precision at the end.
- Chapter 3 is concerned with data reduction and the determination of the excitation spectrum. The extracted spectrum is analyzed and initial results are presented.
- Chapter 4 introduces R-matrix theory, used to extract physical meaningful level parameters by fitting to the extracted excitation spectrum. Two analyses are made, the first being a comparison to a previous similar experiment. The second is an analysis of the 2^{+} doublet, using only the upper part of the spectrum.
- Lastly, Chapter 5 concludes the thesis and looks to the future with suggestions for improvements and further analysis.

Acknowledgements

First, I would like to thank my two supervisors Karsten Riisager and Oliver S. Kirsebom for their competent supervision. They have spent copious amounts of time discussing and guiding me through the process of writing this thesis, and for that I am grateful.

Thank you to Michael Munch who has patiently provided invaluable help, when I have come to him with questions regarding AUSAlib and ORM. Without his help, this work would not have been possible.

I would also like to thank Hans O.U. Fynbo and Jesper Halkjær for providing valuable input in discussions and always being willing to help me. It has truly been an enjoyable experience to work in the Aarhus Subatomic group this past year.

Lastly I would like to thank my family for their love and support. In particular my beloved girlfriend, Asta, for believing in me and always being supportive.

Andreas Møsvraa Gaarde Gad
Aarhus, June 2018

Contents

Chapter 1

Introduction

1.1 Motivation

Nuclear physics is primarily concerned with studying the constituents and interactions of atomic nuclei and nuclear matter. It first branched out from atomic physics in the late 1890s when Henri Becquerel discovered radioactivity. Since then, it has become one of the major research fields within the field of physics, with applications ranging from medicine to nuclear energy. The atomic nucleus is a unique example of relatively few particle systems displaying both single-particle and collective motions, and the interactions are governed by three of the four fundamental forces of nature.

Over the last few decades, the study of light atomic nuclei has experienced a renaissance due to experimental and theoretical developments. There are several experimental factors allowing for more precise studies than previously possible. The development of radioactive beams allows for the creation and subsequent study of specific isotopes with lifetimes down to the millisecond range, which was previously not possible. This technique, known as Isotope Separation On-Line (ISOL), was first developed in 1951 by O. Kofoed-Hansen and K.O. Nielsen for the Copenhagen Cyclotron. It is now used at many facilities around the world, with arguably the prime facility being ISOLDE at CERN.

Not only isotope separation has experienced significant developments, but also detection techniques. Double-sided Silicon Strip Detectors (DSSDs) provide both high energy and spatial resolution, allowing for detailed kinematics and coincidence analyses.

From a theoretical standpoint, the study of light atomic nuclei is also an extremely interesting field. Advanced nuclear models and massive computational power have allowed theoreticians to describe light nuclei in unprecedented detail. This is done using *ab initio* calculations, which solve the many-body Schrödinger equation for realistic nucleon-nucleon interaction potentials obtained from nuclear scattering experiments. Two models in particular have advanced tremendously in recent years. These are the Green's function Monte Carlo (GFMC) [Wir+13] and the No Core Shell Model (NCSM) [BNQ13]. Due to the complexity of the nuclear force, it has thus far only been possible to calculate excited states of light nuclei with $A < 20$, and even these are often not in agreement with experiments. A paper published by Wiringa *et al.* in 2013 [Wir+13] was able to determine the excitation spectrum for ^{8}Be up to 20 MeV, with level energies agreeing with experimental data within a few hundred keV. Due to its many different structures (see Section 1.3) and large continuum contributions, ^{8}Be is a unique test for *ab initio* calculations. To validate the calculations, precise measurements of the experimental spectrum are imperative. Even though ^{8}Be is one of the most well-studied of all isotopes, controversy remains concerning the exact spectrum.

The work presented in this study is based on data from the experiment IS633 performed in May 2017. The experiment was conducted with the ambition of measuring the excitation spectrum of ^{8}Be below 18 MeV in unprecedented detail. Of particular interest is the 16.922 MeV state which has previously been measured only once through β-decay of ^{8}Be with merely five counts, and the so far unobserved electron capture delayed proton emission through the 17.640 MeV state. The experiment was conducted at the ISOLDE facility at CERN by the Madrid-Aarhus-Göteborg ISOLDE (MAGISOL) collaboration, with myself as a lucky participant.

1.2 Nuclear decays

The probing method used in this experiment is the β-delayed $\alpha - \alpha$ breakup of ^{8}B through an intermediate excited state in ^{8}Be. In order to understand the underlying resonance structure in ^{8}Be, a brief review of the relevant decays will be given in this section.

1.2.1 β-decay

Light unstable nuclei generally decay by either proton/neutron emission or β-decay. Only those that are far away from the valley of stability will decay by proton/neutron emission, while those closer decay mainly by β-decay. β-

decay is a weak interaction process of which there are three main types. We will focus on β^+ and β^--decay in this section and treat electron capture separately in Section 1.2.3. The two processes can be described as:

$$\beta^+ : \qquad p \rightarrow n + e^+ + \nu_e \tag{1.1}$$

$$\beta^- : \qquad n \rightarrow p + e^- + \overline{\nu}_e, \tag{1.2}$$

where β^+ turns a proton into a neutron, positron and electron neutrino, and β^- turns a neutron into a proton, electron and anti-electron neutrino. Nuclei below the valley of stability will decay by β^-, while the nuclei above decays by β^+, thereby inching closer to the valley of stability.

The energy available in these decays, the Q-value, is given by:

$$Q_{\beta^+} = M(A,Z)c^2 - M(A,Z-1)c^2 - 2m_e c^2 \tag{1.3}$$

$$Q_{\beta^-} = M(A,Z)c^2 - M(A,Z+1)c^2, \tag{1.4}$$

where $M(A,Z)$ is the atomic mass of an atom with Z protons and A nucleons. The binding energy of the electrons has been neglected in these equations. The Q-value is the mass difference between the initial and final product, and can be distributed between the final products as either excitation energy or kinetic energy.

Allowed β-decays can be divided into two types, depending on whether the interacting nucleon changes spin. If the spin is unchanged, it is a Fermi transition, and if the spin does change, it is called a Gamow-Teller transition. *Allowed* decays are transitions with $L = 0$, and *forbidden* decays are those with $L > 0$, where L is the orbital angular momentum. The nuclear part of the β-decay operator, for allowed decays is:

$$\mathcal{O}(\beta^\pm) = g_V \sum_{j=1}^{A} \tau_\mp(j) + g_A \sum_{j=1}^{A} \sigma(j)\tau_\mp(j), \tag{1.5}$$

where σ the spherical component of the Pauli spin matrices and $\tau_\mp$ are the isospin step operators. The first term corresponds to the Fermi operator and the second to the Gamow-Teller operator. Selection rules for each type of decay can be deduced from these operators. For Fermi decays, the spin, isospin and parity must all remain unchanged. For Gamow-Teller transitions, we have the following rules: $\Delta J = 0, \pm 1$, $\Delta T = 0, \pm 1$ and $\Delta\pi = 0$. The change in spin is coupled to the spin of the outgoing leptons, so their spin has to couple to one. An exception for the Gamow-Teller rules is the $0^+ \rightarrow 0^+$ transition, because spins of one and zero cannot couple to zero. Such a decay is pure Fermi type. Forbidden β-decays are generally 4-5 orders of magnitude slower than allowed transitions,

and their contribution is therefore only significant when no other transitions are allowed.

Due to the selection rules, only a subset of the levels are actually populated in the decay of ^{8}B. In the present study, these selection rules allow us to analyze the spectrum by including only a few levels in the analysis. As the selection rules and couplings are different for other types of decay, the resulting spectra for different probing mechanisms will generally not be the same.

The selection rules for Fermi decays only allow for so-called *superallowed* decays between two *Isobaric Analogue States* (IAS). The IAS are states with a very similar structure, with the only difference being that a proton is changed to a neutron or vice versa. These states are due to the charge independence of nuclear forces, and the energy difference between two IAS is solely due to the added Coulomb interaction in the state with one extra proton. Fermi decays are therefore only energetically allowed for β^+, where there is one less proton in the daughter nucleus.

1.2.2 *ft*-values and strength functions

The intensity of a β-decay transition can be expressed in terms of the *comparative half-life* (ft-value), which is the product of the partial half-life ($t_{1/2}$) and the phase space factor (f). The phase space is the density of final states and is a dimensionless integral over the decay window. Far from the endpoint of the β-window, the phase space can be approximated by:

$$f \simeq \frac{(Q - E_x)^5}{30(m_e c^2)^5}, \tag{1.6}$$

where E_x is the excitation energy. For a more general parametrization for all energies, see [WM74].

The ft-value is directly related to the nuclear matrix elements [BB08] as:

$$ft = \frac{C}{B_F + (\frac{g_A}{g_V})^2 B_{GT}}, \tag{1.7}$$

with

$$C = \frac{\ln 2 \pi^3 \hbar^7}{g_V^2 m_e^5 c^4}, \tag{1.8}$$

where g_V and g_A are the vector and axial vector coupling constants respectively. C is a constant and $B_{GT} = |M_{GT}|^2$ and $B_F = |M_F|^2$ are the matrix elements squared. Present values for the constants C and g_A/g_V are found in [TH10] to be

$C = 6144.2(16)$ and $|g_A/g_V| = 1.2694$. The ft-value ranges from 10^3 to around 10^{20}, with the lower values corresponding to allowed decays.

The Fermi strength , B_F, can be evaluated directly without having to know the explicit wave function. For $\beta^{\pm}$-decay it is:

$$B_F = \left| \langle J_f, M_f, T_f, T_{3f} | \sum_{j=1}^{A} \tau_{\mp}(j) | J_i, M_i, T_i, T_{3i} \rangle \right|^2, \tag{1.9}$$

$$= T_i(T_i + 1) - T_{3i}(T_{3i} \mp 1), \tag{1.10}$$

where T_i is the initial state isospin, and T_{3i} is the third component of the initial state isospin.

The Gamow-Teller strength is not as easily calculated. One can define the Gamow-Teller strength function, $S_{\pm}(GT)$, as the total Gamow-Teller strength summed over all final states:

$$S_{\pm}(GT) = \sum_f B_{f,GT}(\beta^{\pm}), \tag{1.11}$$

where f is the final state. By inserting the Gamow-Teller operator, one can obtain the Ikeda sum rule [Hyl10]:

$$S_+(GT) = S_-(GT) + 3(N - Z), \tag{1.12}$$

which for the case of ^{8}Be becomes $S_+(GT) = S_-(GT) + 6$. As we do not know $S_-(GT)$, this only gives us a lower limit. However, typically $S_+(GT) \gg S_-(GT)$, so we expect $S_+(GT) \approx 6$.

1.2.3 Electron capture

As mentioned previously, the nucleus can also decay by electron capture (EC). Generally speaking, all nuclei that can decay by β^+-decay can also decay by EC. In this process, an orbital electron from the decaying atom is captured and, together with a proton, turned into a neutron and an electron neutrino:

$$EC: \qquad p + e \rightarrow n + \nu_e, \tag{1.13}$$

with

$$Q_{EC} = M(A, Z)c^2 - M(A, Z - 1)c^2. \tag{1.14}$$

The Q-value for EC, is seen to be $2m_ec^2$ larger than that of β^+. The selection rules for EC are the same as for β^+-decays. The transition rates for β^+-decays

are much higher than for EC, and for low excitation energies, the contribution from EC is therefore irrelevant. However, near the endpoint of the β^+-decay window, the phase space of β^+ approaches zero, and EC becomes the dominant contribution. Above the β-decay window, only EC is energetically allowed.

The matrix element for EC is the same as for β^+-decay, so we write the phase space as:

$$f(Q - E_x) = f_\beta(Q - E_x) + f_{EC}(Q - E_x). \tag{1.15}$$

The phase space for electron capture from the innermost atomic shell for allowed decay and in the non-relativistic limit, can be calculated from the expression given in [JW52]:

$$f_{EC} = 2\pi\alpha^3 Z'^3 \left(W_0 + 1 - \frac{1}{2}\alpha^2 Z'^2\right)^2, \tag{1.16}$$

where $\alpha \simeq 1/137$ is the fine structure constant, $W_0 = (E_0 - E_x)/m_e$ is the β endpoint in electron masses with E_0 =17.4688 MeV and $Z' = Z - 0.3$ is the effective nuclear charge, where 0.3 corrects for screening effects by the atomic electrons.

1.2.4 α-decay

α-decay, where the parent nucleus emits an α particle, is by far the most common type of cluster decay with Q-value:

$$Q_\alpha = M(A, Z)c^2 - M(A - 4, Z - 2)c^2 - M_\alpha c^2. \tag{1.17}$$

This type of decay is usually only possible for heavy nuclei, and ^{8}Be is the only known light nucleus that decays primarily by α-decay.

α-decay is fundamentally a quantum tunneling process. The width of the level is inversely related to the lifetime as:

$$\Gamma = \hbar/\tau. \tag{1.18}$$

The observed width of a resonance can be expressed as a product of the penetration factor, P_L, and the reduced width amplitude, γ:

$$\Gamma = 2P\gamma^2. \tag{1.19}$$

The reduced width amplitude is calculated as the final and initial state inner product, integrated over a spherical surface with radius a_c. The radius is called

the channel radius and will be discussed in more detail in Section 1.4 and Chapter 4. The penetration factor is the product of the penetrability function and the phase space. The phase space is a kinematic factor, like the phase space for β-decay. The penetrability factor is the probability that an α particle can escape the nucleus by quantum tunneling through the Coulomb and centrifugal barrier.

For more details on calculations of the penetration function, see Appendix 1 of [Hyl10].

1.3 Nuclear structure of ^{8}Be

Figure 1.1 shows the excitation spectrum for ^{8}Be, with the levels adopted in [Til+04] that are energetically accessible from the ground state of ^{8}B. The spin, parity and isospin is written as $J^\pi : T$ for each level. The ground state of ^{8}Be is situated 92 keV above the $\alpha - \alpha$ threshold.

Density distribution calculations in [Wir+06] of the ground state and the two first excited states of ^{8}Be show, that they all have a large $\alpha - \alpha$ component. This means that these levels can, to a high degree, be understood as two interacting α particles. As a result of this, the reduced width amplitude, γ, in Eq. (1.19) is very large, which is the reason why the two excited states are so wide. The ground state has an observed width of only 5.6 keV, which is counterintuitive. However, this is caused by the vanishing penetrability for low energies. The large overlap with the $\alpha - \alpha$ wave function is of great astrophysical interest, because it is needed to explain how ^{12}C is created in the reaction $^8\mathrm{Be}(\alpha,\gamma)^{12}\mathrm{C}$ through the famous Hoyle state.

β transitions from the ground state of ^{8}B to the ground state and second excited state of ^{8}Be are second forbidden due to the selection rules listed in Section 1.2.1. Decay through the 17.6 MeV level is extremely suppressed[Kir10] and is known to decay by proton emission. The β-delayed $\alpha - \alpha$ breakup of ^{8}B therefore provides a clean probe of the 2^+ levels in ^{8}Be. When measuring the 2^+ doublet, this is of great advantage since the 3 MeV level is the only "contaminant" contribution.

The two close lying 2^+ isospin doublet levels at 16.626 MeV and 16.922 MeV are known to be nearly maximally mixed in isospin. Isospin mixing is treated in an article by P. Brentano [Bre96], where it is shown that the doublet can be described by two interacting isospin eigenstates that experience energy repulsion and width attraction. The $T = 1$ eigenstate is the IAS of the ^{8}Li and ^{8}B ground states, and the matrix element for this transition is therefore very large. However, the β^+-decay window has an endpoint situated just 332 keV and 36 keV above the doublet levels respectively. As the β-decay phase space grows with the fifth power of the β energy, the spectrum is highly suppressed at high excitation

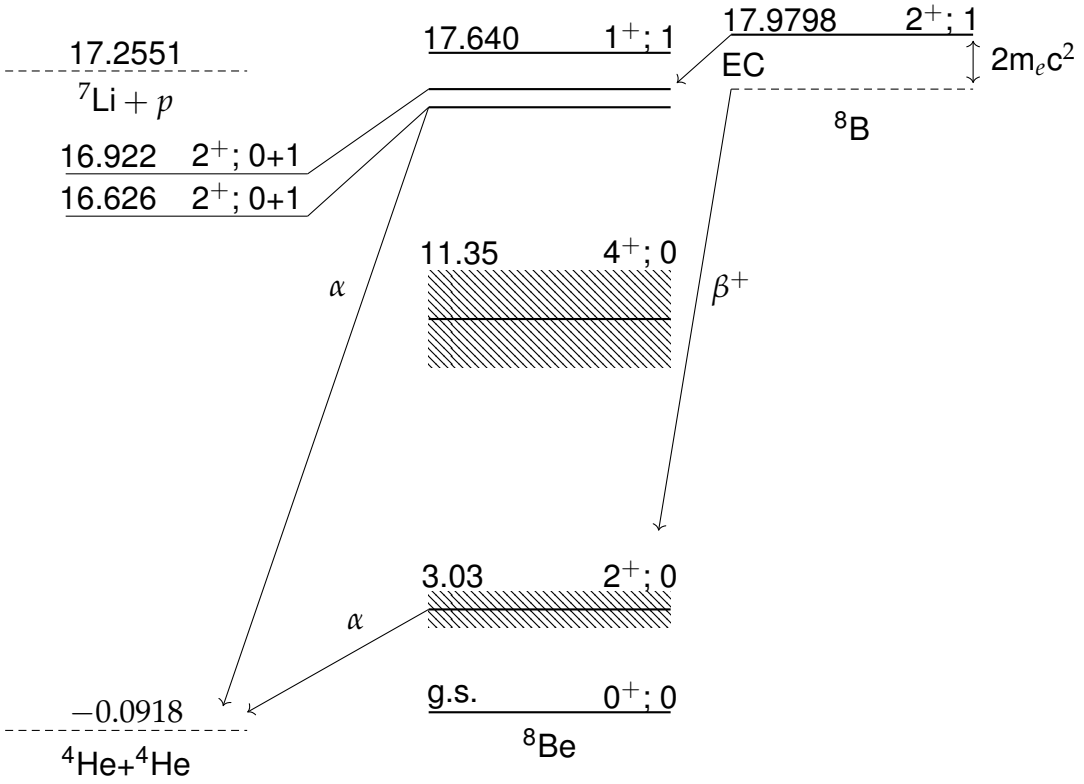

Figure 1.1: Decay scheme for β decay of ^{8}B to known levels in ^{8}Be. Each level is labeled with the energy above the ^{8}Be ground state in MeV. The spin, parity and isospin are labeled as $J^\pi : T$. The 2^+ doublet levels at 16 MeV are known to be strongly mixed in isospin. All energies and quantum numbers are acquired from [Til+04].

energies. Previously, only one experiment has been able to detect decays into the 16.922 MeV level through β-decay of ^{8}B, with only five counts. This experiment was conducted at the IGISOL facility of the Jyväskylä Accelerator Laboratory in Finland in 2008 and is described in [Kir10].

The 2^+ doublet in ^{8}Be is the only known case with more than a few percent isospin mixing, and ^{8}Be is therefore an exceptional case for studying this effect. An improved measurement of this decay with better statistics would allow the testing current assumptions in the treatment of the 2^+ doublet.

^{8}B is known to possess a proton halo structure in its ground state, and is the only known nucleus to do so [Jon04]. Halo nuclei are characterized by a large spatial extension, which is explained by one or two loosely bound nucleons. The halo structure is seen experimentally by breakup reactions. These reactions show an unusually large one-proton removal cross section, and a narrow momentum

distribution of the resulting ^{7}Be fragment, which indicates a large spatial extension [Sme+99]. At 17.640 MeV above the ^{8}Be ground state, we find the only level above the β-decay window and still energetically accessible from ^{8}B. This level is populated by EC, and is known to decay mainly by proton emission. This decay is highly interesting as a probe of the halo structure of ^{8}B. It is believed that the main strength of the EC decay can be described as proceeding separately for the core and the halo proton. In this model, the halo proton acts merely as a spectator, while the strength of the decaying core can be estimated from the known β-decay of ^{7}Be. The EC delayed proton decay through this state has not yet been observed. The detection of this decay was one of the hopes for the experiment IS633, but will not be treated in this study, as it is the subject of the PhD dissertation by S. Onsés from the University of Madrid and part of the MAGISOL collaboration. Also, because of the high trigger levels in this experiment (discussed in Section 2.5.6), a new experiment was conducted in April 2018 with the specific goal of measuring the delayed proton branch. The analysis of this experiment is not yet finished at the time of writing.

1.4 Intruder states in ^{8}Be

Defining a level in nuclear physics is not as straightforward as it sounds. Even though ^{8}Be is one of the most studied isotopes, there is still an ongoing discussion about the existence of broad 0^+ and 2^+ levels at around 6 MeV and 9 MeV. These states were first proposed by Barker in 1968 and 1969 [Bar68; Bar69]. To describe the nuclear resonances, he used a theoretical framework called R-matrix theory, first developed by Lane and Thomas in 1958 [LT58]. R-matrix theory will be described in more detail in Section 4.1, but for now, we will just introduce some of the details. R-matrix expresses the cross section in terms of physical parameters such as the energy, width and feeding parameters for included levels. However, the expression also depends on the channel radius, which is not as clearly determined. The radius determines the border between the internal and external regions, governed by nuclear and Coulomb forces respectively.

Barker argued that to give a consistent description of a resonance, only the feeding parameters must change for a given level, when probing through different feeding mechanisms. To examine the 2^+ states in ^{8}Be, simultaneous fits were made with data from $\alpha - \alpha$ scattering, ^{9}Be$(p,d)^8$Be, and β-decay of ^{8}Li and ^{8}B. When only considering one type of measurement, he found that the level parameters varied with choice of channel radius, all resulting in reasonable fits. However, when simultaneously fitting all datasets and letting the feeding parameters vary between them, the channel radius converged to an optimal value and constrained the energy and width parameters [Bar69]. The resulting

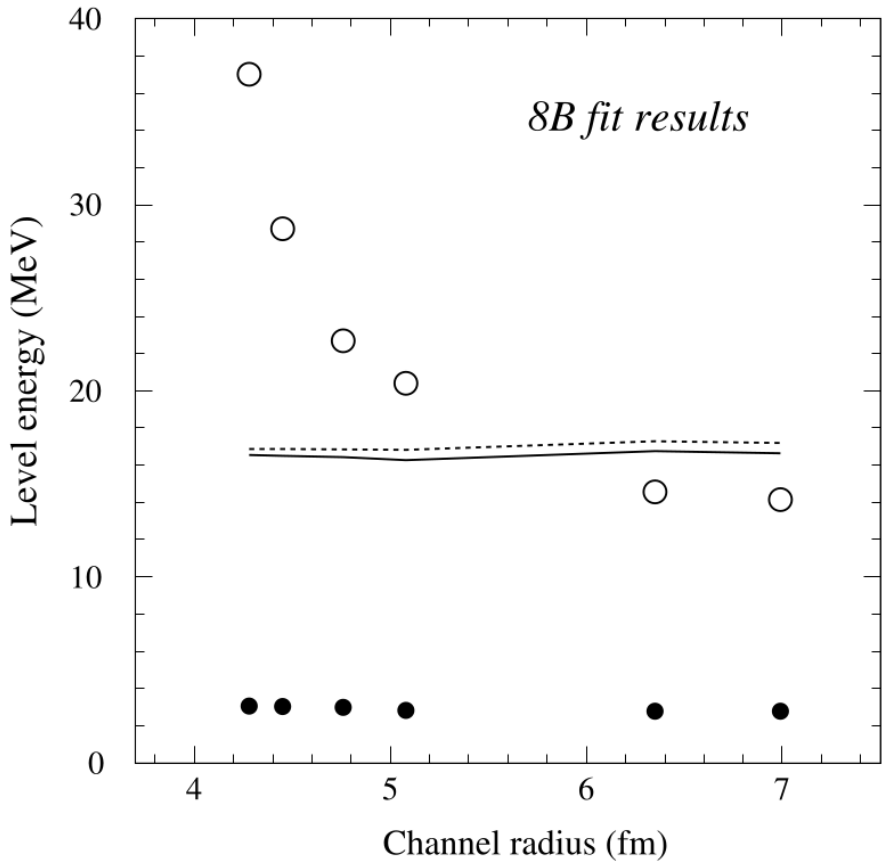

Figure 1.2: The observed energies of the fitted levels from an R-matrix four-level fit of the β-delayed α-spectrum from the decay of ^{8}B. The energies are shown as a function of the channel radius used for the fit. The energies of the well known 3 MeV (black circles) and 2^+ doublet (lines) are shown to be constant, while the position of the fourth level (open circle) varies. This figure is based on data from [Kir10; Hyl10] and is taken from [Rii+15]

states at 6 MeV and 9 MeV are interpreted as intruder states within the shell model, i.e., states belonging to a higher shell configuration.

Several critics have disputed Barker's results [War86a; Fay+98; BA02; BAS06a]. One of the points of criticism, is that none of the proposed intruder states show as a peak in the spectra. Also, there were no constraints on the channel radii used in this analysis, and the fits made by Barker used channel radii larger than 6 fm. Warburton [War86a] argues that the natural choice of channel radius for ^{8}Be should be approximately 4.5 fm based on electron scattering experiments.

A combined fit to 11 difference reactions leading to the ^{8}Be intermediate state

analyzed in [Pag05], supports Barkers 2^+ intruder state. Here the state was found at 16.4 MeV with a width of 19.2 MeV. In this study the channel radii were chosen rather arbitrarily, ranging from 3 fm to 6.5 fm. In other works there was found no need for intruder states [War86a; BAS06a], but here the fits were done separately on different probing mechanisms.

Theoretical *ab initio* calculations have not found any extra low energy 2^+ state for ^{8}Be [Wir+13], which further disputes the existence of the intruder state.

The reason the choice of channel radius may be important is that real physical levels in R-matrix theory should have constant parameters for varying channel radii. However, if the level actually describes non-resonant effects, it may show a significant dependency of the channel radius. Non-resonant contributions to the spectrum may be due to direct continuum decays: that is, decays where the assumption of an intermediate state in ^{8}Be is not valid. Such decays are not treated in R-matrix theory, but may be taken into account by adding an additional high energy level. The presence of such decays can be indicated in a few ways [Rii+15], which can be summarized as: R-matrix levels that do not correspond to any physical "peak" in the spectra; level energies that scale inversely with the channel radius; or levels that have unphysically large values of parameters that represent coupling to different channels, such as the feeding parameter or width. Figure 1.2 is taken from [Rii+15], and shows the fitted energies of a four-level R-matrix fit to the β-delayed α-spectrum from ^{8}B. This level is shown to be in agreement with Barker's model, with a level at approximately 14 MeV when using a channel radius above 6 fm. However, the fits for lower channel radii show that this level should likely not be interpreted as a physical level.

1.5 AUSAlib

The analysis in the present study is based on the AUSAlib[MHK17] program packages, which is based on ROOT[CER16]. AUSAlib stands for Aarhus Subatomic Library, and is a framework formalizing many standard procedures regarding the data analysis of experimental nuclear physics. The library has been developed in the Subatomic group at the Department of Physics and Astronomy at Aarhus University, primarily by M. Munch, O.S. Kirsebom and J. Refsgaard. Various parts of AUSAlib will be explained throughout the thesis in the relevant sections.

Chapter 2

Experimental Methods

The goal of this experiment is to examine the β^+-decay of ^{8}B, with the aim of determining the beta strength for decays into exited states in ^{8}Be. With the half-life of ^{8}B being (770 ± 3) ms, it is necessary to produce the isotope at the same location as the detector setup. Recently new targets at ISOLDE has been able to produce unprecedented yields of ^{8}B, which make ISOLDE an ideal location for this experiment.

The following chapter will be concerned with the experimental approach and calibrations. A presentation of the radioactive beam production and detection setup is given in Sections 2.1 and 2.2. Section 2.3 gives a brief description of the measured data and the structure of it, and a discussion of energy-loss calculations used in the analysis is given in Section 2.4. Various aspects of the calibration and detector response are analyzed in Sections 2.5 and 2.6. Finally a discussion of the energy precision in the experiment is presented in Section 2.7.

2.1 Radioactive beam production

The Isotope Separator On-Line DEvice (ISOLDE) is a part of the larger CERN facility. CERN is located on the Swiss-French border right outside Geneva. CERN is the largest high energy physics facility in the world, with more than 2500 employed staff members, and host of more than 12000 scientific researchers per year. The facility consists of several accelerators, which are connected as shown in Fig. 2.1. The largest accelerator is the Large Hadron Collider (LHC) at which the Higgs boson was famously measured in 2012.

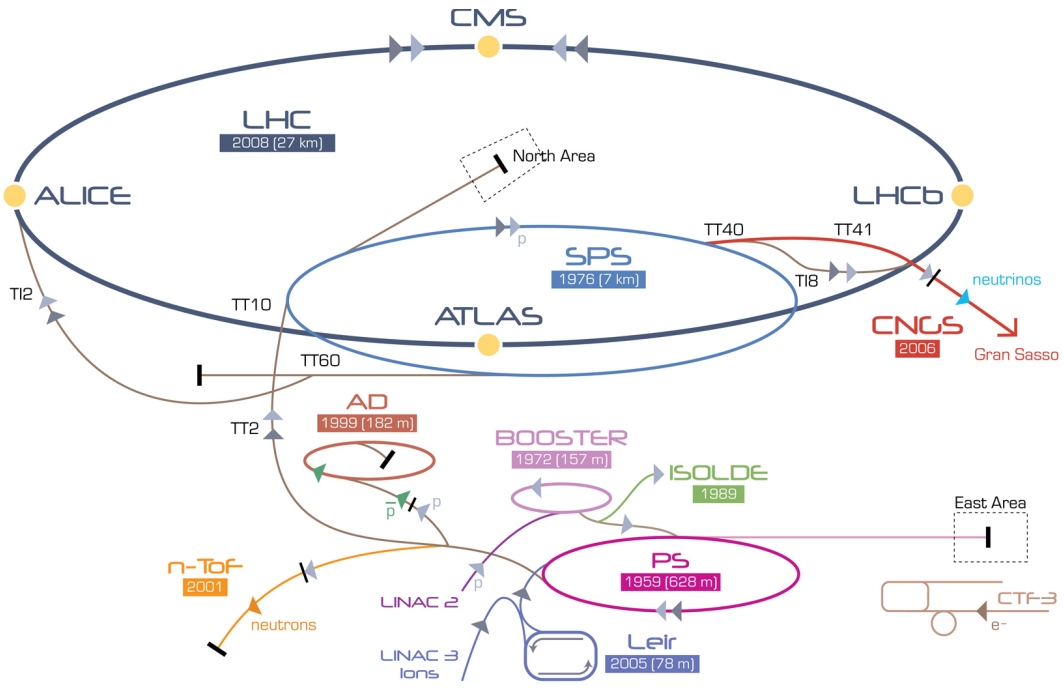

Figure 2.1: Schematic overview of the accelerators and some of the experiments at CERN. The protons used in ISOLDE (green) is accelerated from LINAC 2 (purple), into the PS Booster (light purple) and lastly transported to the ISOLDE facility. This figure is provided by CERN.

The proton beam line used at ISOLDE to produce nuclei, starts at the linear accelerator LINAC 2 which accelerates a bunch of protons to 50 MeV every 1.2 s. They are then led into the Proton Synchrotron Booster (PSB), which consists of four superimposed synchrotron rings, where each ring gets every fourth proton bunch, and accelerates them to 1.4 GeV. Finally these proton bunches are then send to either the Proton Synchrotron (PS) or to ISOLDE. During the experiment approximately half of these proton bunches were directed to ISOLDE. A schematic overview of the ISOLDE facility is seen in Fig. 2.2.

The proton beam is then directed into a cylindrical target with 1.5 mm diameter made of 99 % porous graphite (nanotubes). When the protons bombard the target, spallation, fission, fusion and fragmentation is induced. These processes produce lighter nuclei than the target material. The target is infused with a SF_6 gas, which is highly reactive. The produces nuclei react with SF_6 to create molecules, which then diffuse out of the target. The molecules are then ionized by a plasma ion source, and led out of the production chamber with a 30.0 kV voltage. Next, the relevant ions are isolated in the General Purpose Separator (GPS) magnet. Ions with the same mass as BF_2 (46.0 u) is separated in

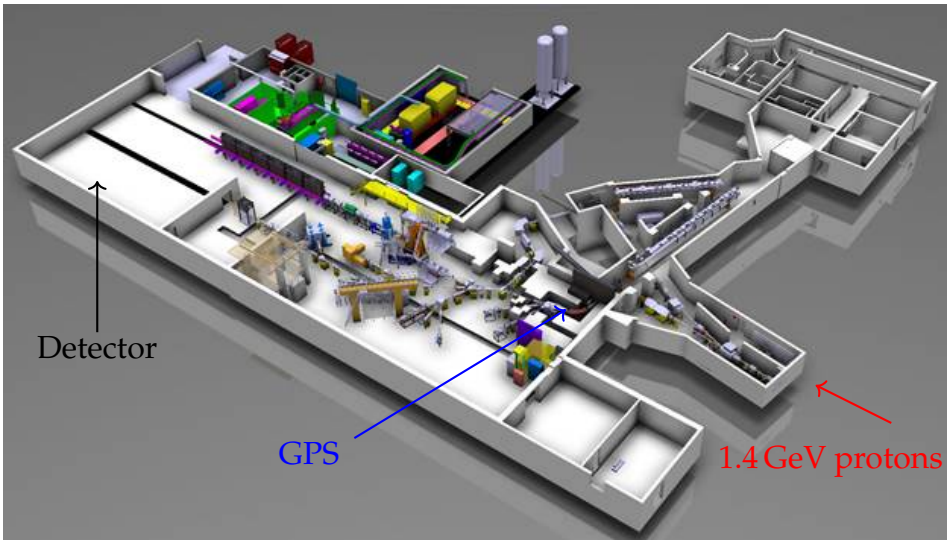

Figure 2.2: Schematic overview of the ISOLDE facility. The red arrow indicates where the proton beam from the PS Booster comes into ISOLDE, and collides with the carbon target. The blue arrow points to the GPS magnet, which separate the nuclei. Lastly the detector setup was in the back of the hall as indicated by the black arrow. This figure is a bit outdated, which is why the area around the detector setup is empty.

this process. In the end, around 10^4 molecules reach the detector setup, out of the original 10^{13} protons per pulse. There are no strong contaminants with the same mass as BF_2, and the beam is therefore very clean.

At the detector setup, the BF_2 beam is collimated through four collimators with widths of 10 mm, 8 mm, 6 mm and 4 mm. The molecules are then implanted with 30 keV into a 137 nm thick carbon target.

2.1.1 Overview of the run

Figure 2.3 shows the time line of the run. In the days leading up to the experiment, calibration runs were made on all detectors. These calibrations were done with a standard α-source with four radioactive isotopes, which we call the 4α-source and will be described later. After the experiment two additional calibration runs were made, one with the 4α-source and one with a ^{226}Ra-source.

During the experiment with ^{8}B beam, the trigger settings were changed constantly in an attempt to improve the yield. The consequences of these changes are discussed in Section 2.5.6. Also at one point there was a 30 min run with the focus of determining the lifetime of ^{8}B. Here, the beam gate closed for 600 ms

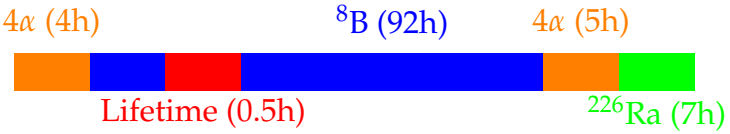

Figure 2.3: Overview of the different measurements done during the experiment. The orange part is calibration runs with the 4α-source. Red block corresponds to the measurements with the beam gate closed for lifetime measurements. Light blue and dark blue are all ^{8}B measurements, with light blue indicating a high detection threshold of 2.5 MeV, while the dark blue is with a lower threshold of 600 keV. The green part indicates the calibration measurement of the ^{226}Ra-source.

in the beginning of every pulse. This was done to prevent excessive overflow, which can have the effect of changing the time distribution.

2.2 Detection system

The detection system used for the IS633 experiment at ISOLDE, included a two different types of detectors. These were Double-sided Silicon Strip Detectors (DSSD), and unsegmented silicon detectors which I from now on will mention as PADs.

As the name suggests, the DSSD is a segmented detector. It measures $5 \times 5\,\text{cm}^2$, and is both sides are divided into 16 strips. The front side is p doped, while the back side is n doped. Each strip is 3.0 mm, and there is an inter-strip width of 0.1 mm made of aluminum. This corresponds to a 97 % coverage of the pixels, and the remaining 3 % covered by the aluminum. The front side p-doped layer is implanted at only 100 nm, which gives the detector a very thin deadlayer of 100 nm. The thickness of the DSSDs used is 40 µm and 60 µm. Figure 2.4 shows an illustration of a DSSD.

The PAD is an unsegmented silicon which is very thick compared to the DSSDs. The PADs used are 1000 µm and 1500 µm, and are used to detect the excess energy of the particles that are not completely stopped in the DSSDs. They are included specifically for detecting protons and electron, but those will not be investigated in this thesis. Information on all the detectors can be found in Table 2.1 and a view of the detector setup is seen in Fig. 2.5.

In this study, we aim to detect alpha-particles in coincidence with a total energy of up to 17 MeV, which means that each alpha will have an energy of up to 8.5 MeV. The fact that we do not have a detector opposite of U5, means that it will not be possible to measure a significant coincidence spectrum with

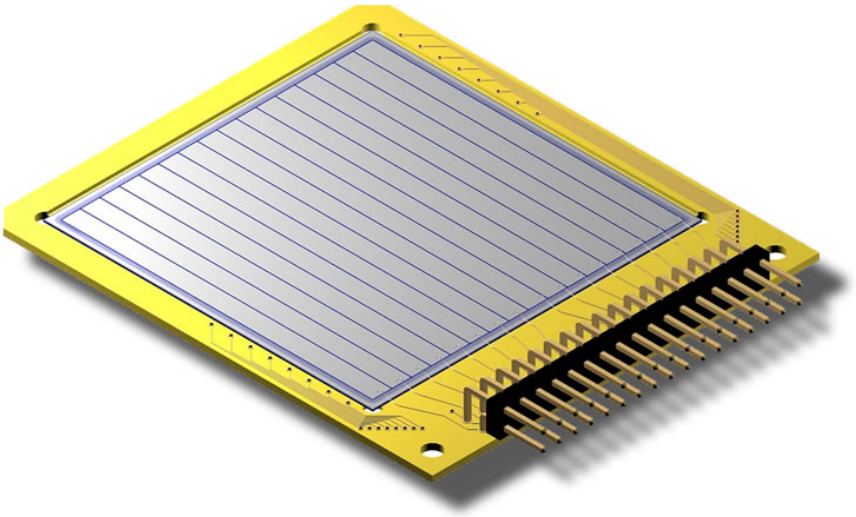

Figure 2.4: Illustration of a DSSD. The detector has 16 p-doped strips and another 16 n-doped strips perpendicular to the other, which creates 256 pixels. Figure is provided by Micron Semiconductor Ltd.

this detector. To detect the protons two thinner DSSD's (U3 and U4) were used. However, these are not thick enough to be able to stop the alpha's with energies above 7 MeV, which is well below the region of particular interest. This means that to measure alpha coincidences in this pair of detectors, we will not only have to match two events in opposite DSSD's, but also their energy deposit in the PAD behind them. This makes the analysis much more complex, and the possibility of detecting false coincidences increases. To counter these two problems, I have chosen only to use events recorded in the DSSD's U2 and U6 in the following analysis. This in turn, will decrease the number of coincidences by a factor of two, and the number of single detections by a factor of $3/5 = 60\%$. However, because the intensity of ^{8}B is so large in this experiment compared to previous similar experiments, we still expect to have enough statistics to see will defined peaks at the 16 MeV doublet.

2.3 Data structure

In this section I will briefly explain how the data is stored and transformed through AUSAlib into ROOT files containing well defined particle events.

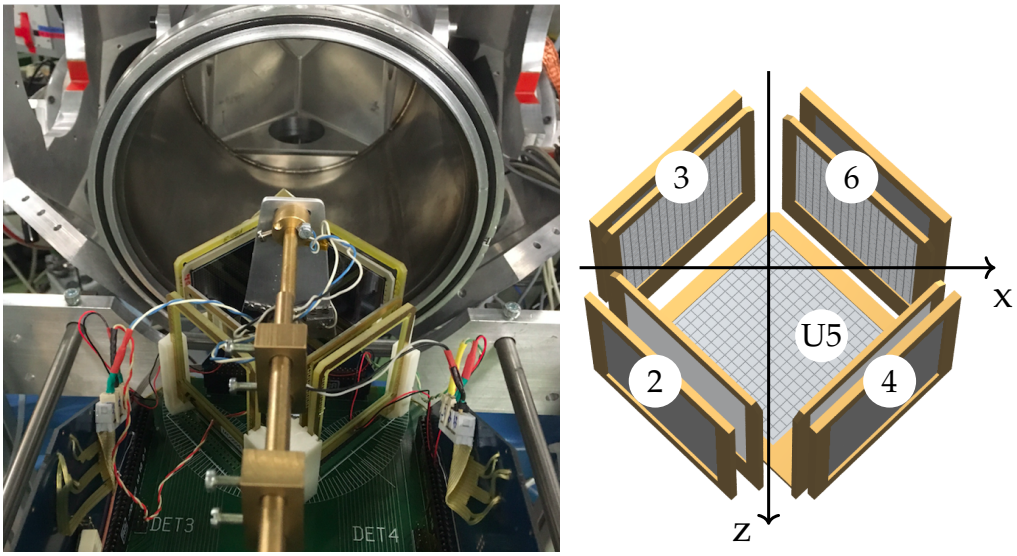

Figure 2.5: (Left) A picture of the detector setup, taken just before the experiment was started. The carbon foil is seen mounted on the telescope in the center. **(Right)** Schematic drawing of the detector setup. The numbers $x = 2, 3, 4$ and 6 signifies the detector pair (Ux and Px), where the DSSSD is closest to the center. The y-axis has not been drawn in this figure to reduce clutter, but a right-handed coordinate system it used, meaning the y-axis points upwards from the center of U5. The target is placed in (0,0,0) and the beam travels along the z-axis.

Table 2.1: Table of relevant information on each detector used in the setup. E_α is the maximum energy α-particle that will be completely stopped in the detector.

Number	Type	Thickness [μm]	E_α[MeV]
U2	DSSD	60	9.13
U3	DSSD	40	7.02
U4	DSSD	40	7.02
U5	DSSD	1000	48.8
U6	DSSD	60	9.13
P2	PAD	1500	61.6
P3	PAD	1000	48.8
P4	PAD	1000	48.8
P6	PAD	1500	61.6

ROOT is a data analysis framework created and maintained by CERN. Data files in ROOT are stored in a TTree structure. A TTree consists of a set of TBranches, where one TBranch corresponds to a variable that is stored, and each variable is either a list or number. Each TTree can hold events that each has their own set of branches, defined by the TTree. This can be seen like a table with rows representing events, and columns representing branches. One of the primary reasons to use ROOT for data analysis, is its capability to efficiently manage extremely large amounts of data. In this experiment we gathered 144 GB data, which makes it necessary to have advanced memory management to handle. Another is that ROOT is created for the specific purpose of creating histograms and is extremely efficient in this task, and has a large toolbox for fitting.

In this experiment an event is started whenever a detector is triggered by a signal larger than its trigger threshold. All signals that are measured in any detector within the next 2.5 µs are then included in this event. Each event has its own set of TBranches defined in the TTree. The raw data files are converted into ROOT files in the AUSAlib "Unpacker" program. In the unpacked ROOT files, we have the following branches:

- DSSD UX, where X= 2, 3, 4, 5, 6 we have:
  - *UXF, UXFI, UXF_E, UXF_T*
  - *UXB, UXBI, UXB_E*

  where F corresponds to the signals from the p-side, and B to the signals from the n-side. UXF is the number of signals (multiplicity) measured in the front strips of UX and vice versa for UXB. I is the strip number, E is the ADC value, and T is the TDC value.

- In the PAD detectors PX, where X= 2, 3, 4, 6 we have:
  - *PXE, PXT*

  where again, E is the ADC value and T is the TDC value.

- global event branches[1]:
  - *TRIGGER* - the id of the triggering detector
  - *TPROTONS* - the time since last proton pulse in units of 10 ns.

[1]There are a few more branches, which I have not included since they will not be used in the analysis.

In these files each signal in either the n- or p-side of a DSSD is treated as seperate events. The next part of the initial analysis is done with the AUSAlib "Sorter". This program has four main purposes:

- Perform energy calibration.
- Do front-back matching of energy signals for double-sided detectors.
- Determine direction of each hit.
- Perform TDC alignment.

To do this step, the user must provide a setup-file, matcher-file, and ADC and TDC calibrations. The setup-file contains properties for the detectors namely geometry, detector-type and dead-layer thicknesses. The matcher-file includes information about energy-tolerances for front-back matching, strips to ignore and high/low energy thresholds for each detector. This is used to remove all events that are due to low-energy noise signals.

2.4 Energy loss of charged particles in matter

Understanding the interaction between charged particles and matter is crucial in all nuclear physics experiments concerned with measuring charged particles. In this study, we measure the energies of alpha-particles through their interaction with the silicon detectors, where large numbers of electron-hole pairs are created. The passage through non-detection material also account for substantial energy corrections in the analysis. To make a precise analysis, we need to understand these effects.

The energy losses associated with the interaction between a charged particle and the material can be divided into electronic and nuclear energy losses. The electronic losses are due to collisions with the atomic electrons which result in ionization or excitation of the atom. The nuclear losses are associated with the transfer of energy to the center of mass movement of the atoms. The energy loss per distance (dE/dx) due to interactions with the material is often called the stopping power. The stopping power can be described with the famous Bethe formula [Sig06]. This equation describes the mean stopping power of swift charged particles (protons, alphas and ions) through matter, and was first derived in 1930. The relativistic version of this equation is:

$$\left\langle \frac{dE}{dx} \right\rangle = \frac{4\pi}{m_e c^2} \frac{NZz^2}{\beta^2} \left(\frac{e^2}{4\pi\epsilon_0} \right)^2 \cdot \left[\ln \left(\frac{2m_e c^2 \beta^2}{I \cdot (1-\beta^2)} \right) - \beta^2 \right], \tag{2.1}$$

where N is the atomic density of the material with Z electrons in each atom, $\beta = v/c$, z is the charge of the particle and I is the mean ionization potential or the average energy needed to ionize the atom. This ionization potential can be

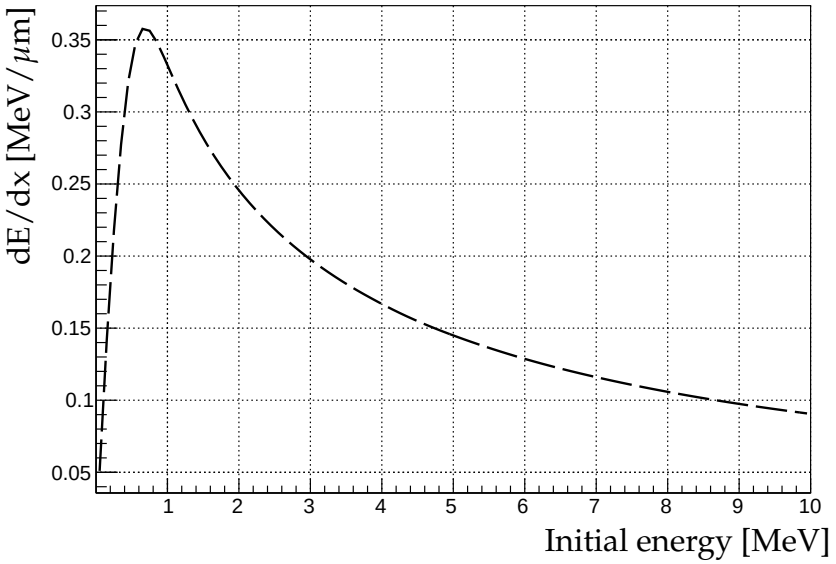

Figure 2.6: SRIM calculation of stopping power of a 0-10 MeV α-particle, traveling through 1 µm Silicon.

found in tables for the particular material used in [ICR93]. Equation (2.1) applies to light charged particles such as protons and α-particles, but not electrons. This is due to the fact that electrons have a very small mass and therefore further relativistic corrections are needed. The formula is only valid for particles with high enough energies that the particle does not carry any atomic electrons with it, luckily this is not a problem at the energies we are concerned with. For particles with velocity $\beta \ll 1$, the logarithm is a slowly varying function, and the stopping power therefore decreases as $dE/dx \propto v^{-2}$ for increasing energies. This is what we see in Fig. 2.6, which show the stopping power for 0-10 MeV α-particles in silicon. For large velocities ($\beta \approx 1$) the relativistic effects come into play and the stopping power starts to increase logarithmically. For α particles this is only important for energies above the order of GeV.

By numerical integration, Eq. (2.1) can be used to calculate the energy lost by a particle when traveling through a material, which is one of two things we might be interested in knowing. The other is the range of the particle, that is the distance a particle with a specific initial velocity on average will travel through a material before being stopped completely. For heavy ions, the path is more or less linear except near the very end of its trajectory. This means that we can write its range as $R = \int_0^R dx$, where we already know dE/dx from equation Eq. (2.1). By inserting this, we an expression for the range of the particle. In reality one

would observe a spread around this range. This is called the *straggeling*-effect and is due to the statistical nature of the problem.

Even the relativistic Bethe formula shown in Eq. (2.1), is not an exact solution. There are correction terms for both high and low energies which is not taken into account yet. Some fo these effects are found empirically, and it is therefore a difficult task to calculate a precise stopping power. This is why I have chosen to use the SRIM (Stopping and Ranges of Ions in Matter) program package[ZZB15; Zie18] to calculate energy losses and ranges. This program is based on Monte Carlo simulations to generate tables with stopping powers, ranges and straggeling as a function of energy for incoming particles on many different materials. Part of the calculations used in this study is made directly in SRIM and some are made in the Eloss routine [Hal18] which is part of AUSAlib and is also based on SRIM tabulated values. For a more in-depth analysis of SRIM calculations and its precision, see section 2.2 in [Kir10].

2.5 Calibration of detectors

The energy calibration of the detectors were done the day before we got beam time. However, it was quickly discovered that there were problems with these calibration files because of an unknown change/drift in the electronics. Therefore another calibration run was done after the experiment ended, which is the one we will use for the following analysis. As mentioned previously, we used two different sources. The first one is a standard source with four alpha emitters, which are ^{148}Gd, ^{239}Pu, ^{241}Am and ^{244}Cm. From here on out, this source will be mentioned as the 4α-source. The second run is conducted using a ^{226}Ra source which decays via the following decay scheme:

$$
\begin{aligned}
^{226}\mathrm{Ra} &\xrightarrow{\alpha} {}^{222}\mathrm{Rn} \\
^{222}\mathrm{Rn} &\xrightarrow{\alpha} {}^{218}\mathrm{Po} \\
^{218}\mathrm{Po} &\xrightarrow{\alpha} {}^{214}\mathrm{Pb} \\
^{214}\mathrm{Pb} &\xrightarrow{\beta^-} {}^{214}\mathrm{Bi} \\
^{214}\mathrm{Bi} &\xrightarrow{\beta^-} {}^{214}\mathrm{Po} \\
^{214}\mathrm{Po} &\xrightarrow{\alpha} {}^{210}\mathrm{Pb}.
\end{aligned}
$$

The energies found in literature for both sources are shown in Table 2.2.

The following section will be concerned with geometry and energy calibrations, as well as investigating the energy thresholds for the detectors.

Source	Radionuclide	Half-life	Energy [keV]
4α	^{148}Gd	71 yr	3182.7
	^{239}Pu	24 000 yr	5155
	^{241}Am	434 yr	5499
	^{244}Cm	18 yr	5805
^{226}Ra	^{226}Ra	1600 yr	4773.4
	^{222}Rn	3.8 d	5489.0
	^{218}Po	3.1 ms	6001.1
	^{214}Po	163 µs	7686.7

Table 2.2: Table of α-emitters used for calibration. The listed energies are found in [Lab17].

2.5.1 Geometry calibration

A figure of the detector setup can be seen in Fig. 2.5. We have some rough measurements of the geometry of the setup from when the experiment was done, but in this section we will use hitpatterns (the number of events in each pixel on the detector) to determine more precise positions of the DSSD's. The analysis was done using the program Geodwim, which is part of the AUSAlib library.

In this part we will use a different coordinate system from the one used to describe the whole detector setup. Here we use a local system for each DSSD, with origin at the calibration source and the center of the detector in (x, y, z), where the x,y-plane is the detector plane and z is normal to the detector plane. In the following analysis, we assume the source to be a point source. Because there is no preferential direction of α emission, we can expect the particles to be uniformly distributed over 4π. This means that the number of events in each pixel on a detector should be proportional to the solid angle of that pixel. If we assume the pixels to be small, the solid angle of each pixel can be written as [Kol15]:

$$\Omega_{i,j} = \cos\theta \frac{a^2}{4\pi R_{i,j}^2}, \tag{2.2}$$

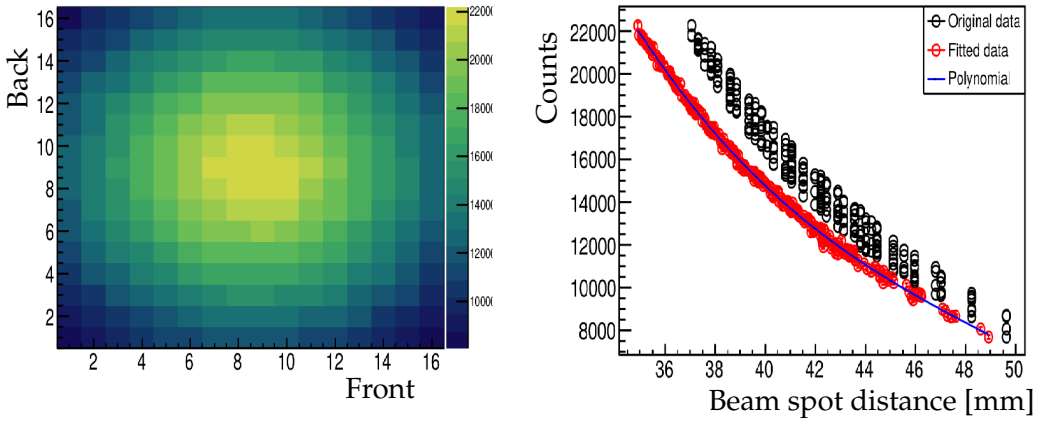

Figure 2.7: (Left) Shows the hitpattern for U2 for a selected part of the ^{8}B run. **(Right)** Shows the corresponding geometry fit. Black circles are the original data based on hand-measured geometry. The red circles are fitted data points and the thin blue line is the fourth order polynomial.

where

$$\cos\theta = \frac{R_z}{r}, \tag{2.3}$$

$$R = \sqrt{R_x^2 + R_y^2 + R_z^2} \tag{2.4}$$

and

$$r = \sqrt{R_x^2 + R_y^2}, \tag{2.5}$$

$$R_x = i(a+b) - c + x, \tag{2.6}$$

$$R_y = j(a+b) - c + y, \tag{2.7}$$

$$R_z = z. \tag{2.8}$$

Here, i and j are the indices of the pixel, r is the distance from the center of the DSSD to the pixel, $a = 3.0\,\text{mm}$ is the strip width, $b = 0.1\,\text{mm}$ is the inter-strip width and $c = \frac{16+1}{2}(a+b)$.

The calibration is then done in four steps.

1. First we find the x and y displacements by fitting the number of hits in each pixel to a fourth order polynomial as a function of r, as described in [Kol15]. This fourth order polynomial is a linear combination of orthogonal polynomial defined in [Bar00]. The coefficients of these orthogonal polynomials are independent of each other, eliminating correlation terms and

therefore making the fit more robust. This method is not sensitive to the distance along the z-direction, which is why we only use this to determine x and y.

2. To find the position along the z direction, we fit:

$$N(i,j) = C\Omega(i,j), \tag{2.9}$$

where C is constant for all indices. This fit is generally not as robust as the previous, but because we already have approximate solutions for x and y, we lock these and find z. This method is known to result in small systematic deviations due to the finite size of the source.

3. Next we do step 2 again, but this time with z locked to the new value. This is used to check if x and y has changed with the new value of z.

4. Lastly step 1 is done again, with the new value of z to check again if x and y are consistent.

This method can be done iteratively, until one finds a stable set of coordinates. Depending on the amount of statistics it may be necessary to use loglikelihood minimization which work well for low statistics tests. In this case we have used the Neyman algorithm.

The position of the target was not necessarily the same during the two calibration runs and the ^{8}B run. The geometry calibration was therefore made individually for each of the three parts of the experiment The hitpattern and corresponding fit from step 4 for U2 using the ^{8}B data, is seen in Fig. 2.7. The other fits are similar, and are therefore not shown. The resulting x,y and z, converted into the global frame, is seen in Table 2.3 for detectors U2 and U6 in the three sets of data. The errors on the position are on the order of 100 µm or below for all coordinates. Solid angles for each detector is also calculated as a percentage of 4π. During the ^{8}B run, we have a coverage of 21%.

2.5.2 Calibration with 4α-source

Calibration of the ADC values for the detectors was done for each front and back strip individually. This is done by measuring a number of different α-decays from the calibration source, then finding the peak positions in terms of channel-numbers, so that we have a channel-number corresponding to a known energy. Lastly a linear fit through these points is made, to get the slope and offset for all individual strips. As mentioned in Section 2.1.1, we did measurements for two different calibration sources, 4α and the ^{226}Ra-source. In this study, I have chosen to only use the 4α-source for making the actual calibrations. There are

Name	Source	x [mm]	y [mm]	z [mm]	Solid angle (%)
U2	4α	-25.1	-3.0	16.1	13.5%
	^{226}Ra	-22.2	-3.2	22.0	12.7%
	^{8}B	-24.1	1.0	24.7	11.2%
U6	4α	23.9	-2.6	-16.1	14.1%
	^{226}Ra	28.7	0.0	-26.0	9.5%
	^{8}B	27.6	2.9	-25.7	9.8%

Table 2.3: Result of geometry calibration determined from ^{8}B, ^{226}Ra and 4α. The coordinates indicate the center of the detector. For the calculation of solid angles the approximation has been used, that they all squarely face the origin.

two main reason do to the calibration in this manner. Firstly, the calibrations are done with the Calibrator tool in AUSAlib. This program takes a root histogram with the channel-spectrum as input, and fits a specified number of Gaussians to the spectrum. It then choses the calibration parameters from a linear fit to the known peak energies versus the channel number found for each peak. In the case of the ^{226}Ra-source, there is a significant angular dependent deviation from the measured peak energies and the ones found in literature. This is due to the fact that ^{226}Ra is implanted into a gold foil, which the leads to significant energy losses in the source itself. AUSAlib has the option to take global energy shifts into account but not angular dependent shifts. This effect is not a problem in the 4α-source, because the implantation depth in the source is negligible. Secondly, the amount of statistics in the two calibration runs differ by three orders of magnitudes. Because some of the ^{226}Ra peaks lie quite close to the much larger 4α peaks, it is not possible distinguish the ^{226}Ra peaks from the rest. Instead we use the ^{226}Ra-source to do a separate check of the calibrations, which will be done in Section 2.5.4.

To calibrate to the 4α-source, we will need to determine the position of each peak in the channel-spectrum very precisely, down to a few keV. To avoid skewing the placement of the peaks due to an asymmetrical response function[2], we will fit a very local Gaussian around the peak. The uncertainty on the peak positions from the Gaussian fits are well below 1 keV, and the residuals from the linear fit are all within 1-2 keV. The mean standard error on the offset and slope of the linear fit are 2.5 keV and 1.3×10^{-3} keV/channel respectively for U2, and

[2]This phenomena will be investigated in Section 2.6.

2.1 keV and 1.0×10^{-3} keV/channel for U6.

2.5.3 Detector deadlayer

On the front and back of the DSSD detectors there is a thin layer of silicon, which does not measure the energy of the alphas. This layer is called a deadlayer and is declared by the manufacturer to be 100 nm thick for the DSSD's, however the precision of this is not specified.

It is usually possible to measure the size of the deadlayer, by measuring a narrow peak and then rotating the detector with respect to the source. This will change the effective distance that the charged particles has to penetrate before being measured. For a thin deadlayer where the energy loss is small enough that dE/dx is approximately constant, the angular dependent energy loss can be found as:

$$dE(\theta) = \frac{dE}{dx}\frac{d}{\cos\theta}, \tag{2.10}$$

where θ is the angle of incidence on the detector and d is the deadlayer thickness. In this experiment we did not do this specific measurement. Attempts were made to measure the deadlayer thickness from other measurements, but this was not successful due to lack of statistics. We will therefore use the declared thickness, to calculate the expected energy loss for each particle we measure and add this. A previous study using the same type of detectors, have found that the declared length is only precise within around 20% [Kir10]. This means that there might be a broadening and systematic angular and energy dependent error due to this. The maximum angle of incidence on the detector is around 80 degrees, and the stopping power is largest for low-energy particles. So for the most extreme cases of a 3 MeV α-particle coming at an angle of 80 degrees, a 10% deviation from the declared thickness is will cause a shift of 11 keV. This effect is somewhat reduced in the calibration and when calculating the implantation depth of the target foil in Sections 2.5.2 and 2.5.5.

2.5.4 Implantation depth of ^{226}Ra-source

The ^{226}Ra-source goes through several steps of decays as shown earlier. However for each step, there will be a recoil of the daughter-nucleus. This recoil means that some of the daughter-nuclei will sputter out of the source, which effectively increases and broadens the implantation depth for each step. To quantify this, we analyze each α-decay individually in an attempt to measure the implantation depth for each decay. This information is then used to perform a check on the 4α calibration in the high energy region.

As mentioned in Section 2.5.3, the energy loss of a particle going through a thin layer can be expressed as:

$$dE(\theta) = \frac{dE}{dx}\frac{d}{\cos\theta}, \tag{2.11}$$

where this time θ is the outgoing angle from the source.

To find the implantation depth for each type of α-decay, we find the peak position as a function of the outgoing angle from the ^{226}Ra-source for each of the detectors U2 and U6. The spectra used in this analysis has been corrected for the 100 nm deadlayer of the detector. The shape of spectra we are trying to fit, are heavily dominated by the detector response functions. This phenomena will be investigated in Section 2.6. For this analysis the peak energies are found by fitting a Gaussian to the area $E_{max} \pm 30$ keV. The reason to use such a narrow Gaussian is because the peak is not symmetric. Instead it has a significant tail towards lower energies which, if included, will skew the fit towards lower energies. This approach is used in order to be consistent with the method used in the calibration with the 4α-source in the previous section.

The found peak energies are then fitted to the following equation:

$$E(\theta) = E_0 + k + \Delta E_0 \cdot \sec\theta, \tag{2.12}$$

where E and E_0 are the measured peak energies and the values found in Table 2.2 respectively, k is a constant allowing for small deviations due to experimental errors, and ΔE_0 is the energy loss for a particle going out of the source at zero degrees. Figure 2.8 shows $\Delta E = E(\theta) - k - E_0$ as a function of $\sec\theta$ for both detectors. The blue lines shows $\Delta E_w \cdot \sec\theta$, where ΔE_w is the weighted average of ΔE_0 for both detectors. There is some systematical trends in the ΔE_0's found in each of the fits. The energy loss is consistently around 4.5 keV larger in U2 than in U6. At this time, we do not understand why we see this effect, but it is suspected to be due to imperfections in the calibration for U6.

The energy shifts are translated into implantation depths, using stopping powers from SRIM, as $d = \Delta E_w/(dE/dx)$. The resulting depths of this analysis are (27 ± 5) nm, (26 ± 5) nm, (32 ± 6) nm and (35 ± 6) nm respectively. Here we see that the effective depth of the source increases for each decay, which is consistent with our expectations. The second depth is a bit smaller than the previous, but this is clearly within the errors of the analysis. The initial implantation depth of 27 nm correspond to an implantation energy of 399 keV.

As a test of these results, a simple Monte Carlo simulation has been made. We determine the starting position of each nuclei using a Gaussian distribution with $\mu = 27$ nm. A SRIM simulation implanting ^{226}Ra into a gold foil with 399 keV, yields a standard deviation of 15 nm of the distribution, due to straggeling. All

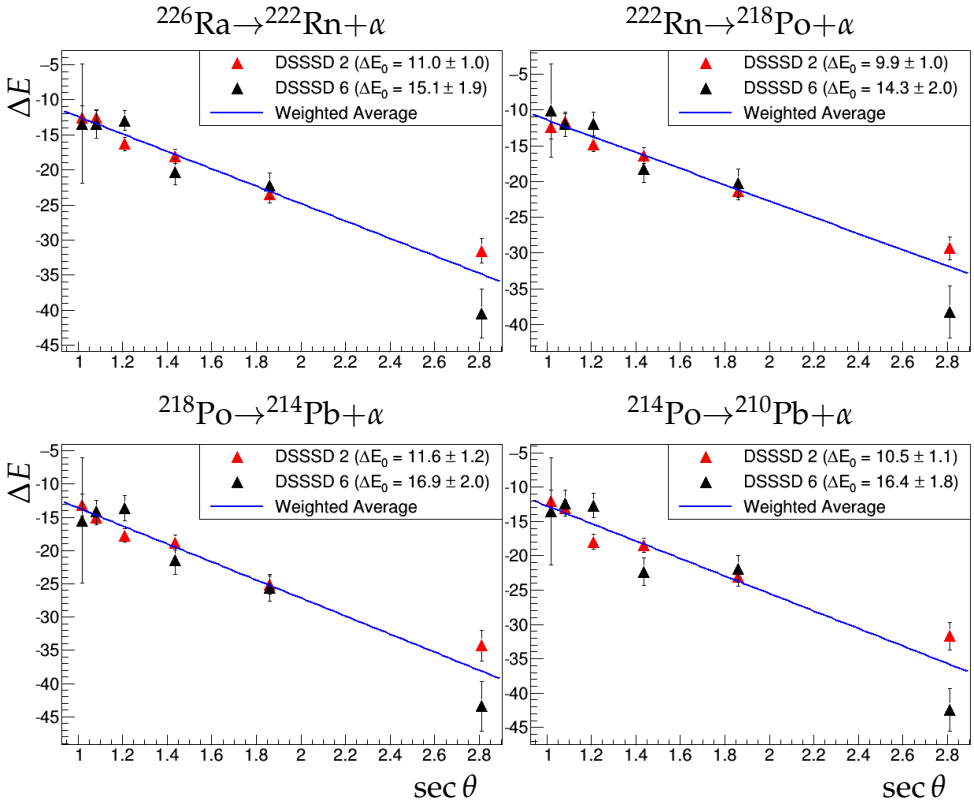

Figure 2.8: Energy loss of α-particles going out of the ^{226}Ra-source.

nuclei are then given a direction drawn from a uniform spherical distribution, and a range drawn from a Gaussian distribution. The mean and spread of the range are also simulated in SRIM. The mean implantation depths after the first decay, based on the simulation are 28.5 nm, 29.0 nm and 29.5 nm. This is obviously not in very good agreement with the experimental analysis. However, the simulation is very dependent on the spread of the starting position, and on both the mean and spread of the ranges for each decay. By changing the standard deviation of the starting position from 15 nm to 18 nm, the simulated depths changes to 29.8 nm, 31.9 nm and 34.0 nm. This is obviously in much better agreement with the experimental measurements. Based on the Monte Carlo simulation, the measured depths seem realistic.

Now that we have investigated the properties of the ^{226}Ra-source, this can be used to do an independent analysis of the energy calibration. We do this by using the newfound source-depths to correct for energy losses through the source. Figure 2.9 shows $\Delta E = E - E_0$, where E is the measured peak energies,

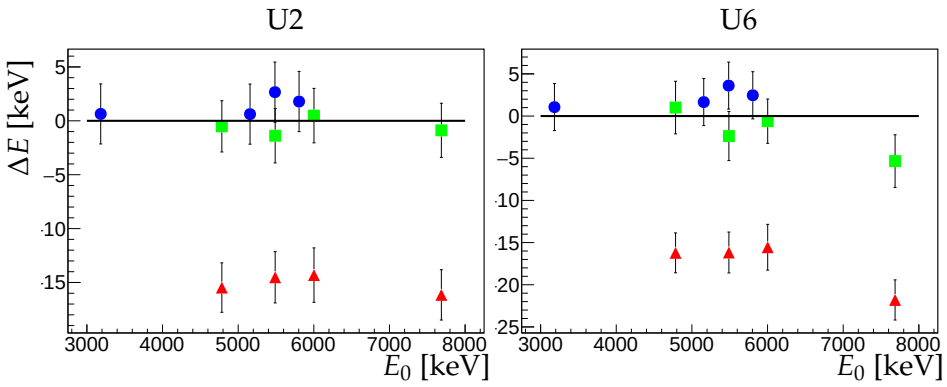

Figure 2.9: Plot of the differences between the measured and literature peak energies. The blue circles are peaks from the 4α calibration source. The red triangles are the peaks measured from the ^{226}Ra-source. The green squares are also from the ^{226}Ra-source, but where each event has been corrected for energy losses through the source. The peak positions are found by fitting a narrow Gaussian to the data.

while E_0 are the values found in Table 2.2. The blue circles correspond to the 4α-source, and it is seen that these differences are generally within the error-bars. However, there is a systematic shift indicating too large dead-layer corrections, and this trend is identical for both detectors. The red triangles are the residual energy for the ^{226}Ra peaks where we have not included the source-correction. Here it is seen that they are shifted t least 15 keV lower than the expected energies. The green squares are the same peaks from ^{226}Ra-source, but here we see that we have successfully corrected for most of the errors associated with energy loss through the source. The results from U2 looks to be correct within a few keV. For U6 though, it seems like there is a downward trend for increasing energy. This is consistent with the differences seen in Fig. 2.8, where the slope is consistently larger for U6. This effect could in part be due to the deadlayer of the detector, which might deviate from the declared value of 100 nm. A way to investigate this, is to uncouple the effect of energy loss in the deadlayer. One way to achieve this, is to only make the analysis in certain pixels where the angle of incidence on the detector is the same. This has been tried, but lack of statistics made this attempt futile.

An estimate of the energy uncertainty at 8 MeV based on this analysis, is 4 keV for U2 and 8 keV for U6. This leads to a uncertainty of 9 keV on the sum energy.

2.5.5 Energy loss in target

The α's measured during the ^{8}B run, are created by implanting BF_2 with 30 keV into a 31 µg cm^{-2} carbon foil which is equivalent to a thickness of 137 nm. The BF_2 breaks upon impact with the foil, and ^{8}B continues with an energy of $8/46 \cdot 30\,\text{keV}$[3]. A simulation in TRIM shows that this gives an implantation depth of 18.9 nm into the foil. This means that the outgoing particles will lose energy:

$$\Delta E_T = E(\theta_T) - E_0 = \delta E - \frac{dE}{dx}\frac{d_T}{\cos\theta_T} \tag{2.13}$$

where E_0 =16 626 keV, θ_T is the angle perpendicular to the carbon foil plane and d_T is the thickness of the foil the particle has to pass. Again, we include δE to take into account small errors in the calibration. α's detected in U6 will have lost energy corresponding to d_T =18.9 nm, while the thickness for α's measured in U2 is 137 nm − 18.9 nm $\simeq$ 118 nm. The implantation depth and total thickness, can be measured just as in the previous section, by measuring the angular dependency of the energy. The hurdle in this analysis is how to determine the energy precisely. In the previous section, we had a narrow peak that could relatively easily determined. This is not the case in the ^{8}B spectrum, as there are no narrow isolated peaks. Instead we use the 16.6 MeV peak. The signal at 16.6 MeV is not symmetric, and we will therefore use a Gaussian folded with an exponential tail towards lower energy and only fit in a range of 80 keV centered around the peak. The energies are then fitted to Eq. (2.13), which can be seen for both detectors in Fig. 2.10.

The results of this fit, gives depths of (17 ± 8) nm and (115 ± 6) nm for U6 and U2 respectively, and a total thickness of (132 ± 11) nm. The implantation depth corresponds very nicely with the simulation made in SRIM and the total thickness is also in agreement with the declared value within the errors. The depths found in this analysis will later be used to to energy-loss corrections for each particle individually.

2.5.6 Detection thresholds

There are two thresholds for both the DSSD's, one for the ADC and TDC. The ADC threshold determines the minimum possible energy that the system will detect and while the TDC threshold determines the lowest energy that detector will trigger on.

[3]The fraction 8/46 corresponds to the mass of ^{8}B with respect to the whole molecule.

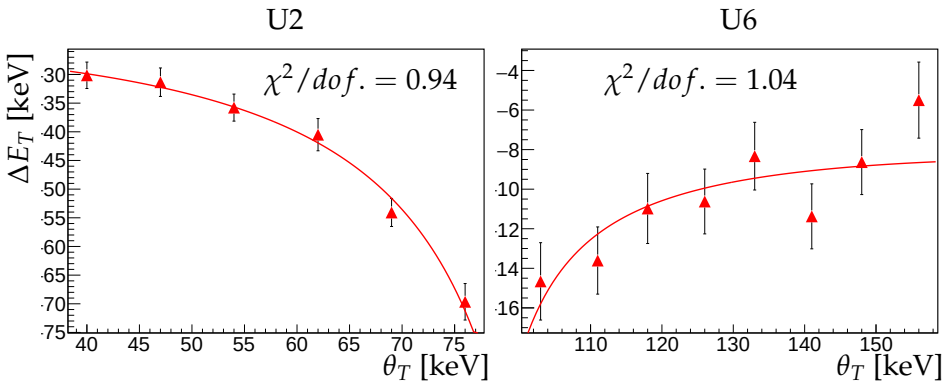

Figure 2.10: Energy loss of α-particles from the 16.6 MeV level in ^{8}B as a function of the outgoing angle from the carbon foil. The energies are found by fitting a narrow Gaussian with an exponential tail.

During the experiment, TDC thresholds were changed several times in an attempt to increase the yield by decreasing the deadtime[4]. The TDC threshold were consistently around 1.5 times larger for U6 than for U2. When doing coincidence analysis, we are therefore limited by the U6 threshold. The lowest threshold settings used for U6 were 1.4 MeV and that was only for a relatively short period of time. The settings used for the bulk of the duration were between 2 MeV and 2.5 MeV. These energies are not corrected for losses in the carbon target and the deadlayer of the detectors, and the actual threshold is therefore a bit higher. As a consequence of this, a conservative 3 MeV cutoff is set for single alphas and 6 MeV for coincidences. This of course means that we cannot investigate the 3 MeV level with this set of data. As we are mostly interested in the doublet this is not catastrophic for the following analysis. However, as we will see later, it becomes a problem when doing R-matrix fits to the entire spectrum.

2.6 Finding the detector response

The response of the detector is the distribution of energies measured from a perfectly monochromatic source. This distribution is referred to as the *"response-function"* and is an intrinsic property of the detector. The response-function will smear out the spectrum and to a lesser degree even change the spectrum we

[4]This is the fraction of time that the setup is not able to detect events due to processing of the signals.

measure from the β-delayed α-decay. To understand the spectrum we see in the end, we therefore need to understand the detectors effect on it.

To measure the detector response, we would ideally need a monochromatic source. As this is not possible, we instead use the α-decay from the calibration measurements. More specifically we look at the 3.183 MeV peak from ^{148}Gd. This peak has a natural width of $\Gamma = 0.024$ keV, which is much smaller than the scale of the detector response. We therefore approximate this peak as a monochromatic source.

Figure 2.11 shows the zoomed in spectrum of the 3.183 MeV peak we are interested in. We clearly see that this spectrum cannot be explained merely by a simple Gaussian, as there is a secondary peak (the so-called *"satellite peak"*) shifted to lower energy than the main peak. This effect is due to α's hitting the narrow 0.1 mm aluminum strips on the DSSD's, which causes them to lose more energy.

A parametrization of the line shape caused by experimental effects have been made in [BAS06b]. The parametrization of the main peak consists of a Gaussian folded with two exponential tails:

$$\psi(E_0, E) = \sum_{i=1}^{2} \frac{A_i}{2\lambda_i} \exp\left(\frac{E - E_0}{2\lambda_i} + \frac{\sigma^2}{2\lambda_i^2}\right) \cdot \operatorname{erfc}\left(\frac{E - E_0 + \sigma^2/\lambda_i}{\sqrt{2}\sigma}\right), \qquad (2.14)$$

where A_1 and A_2 are normalization constants, E_0 is the main peak energy, λ_i is the exponential tail lengths, σ is the width of the Gaussian and $\operatorname{erfc}(x) = \frac{2}{\sqrt{\pi}} \int_x^\infty \exp(-t^2)dt$ is the complementary error function.

We can include the satellite peak as has been done in [Kir10] by adding a Gaussian distribution with width σ_g and energy E_g folded with ψ. For simplicity I have chosen just not to fold the secondary Gaussian with ψ. This takes away the "tails" of the satellite peak, but as area of the satellite peak is only around 3% of the main peak this is a very small correction. The resulting response function is then:

$$\Psi(E_0, E) = \psi(E_0, E) + \frac{A_g}{\sqrt{2\pi}\sigma_g} \exp\left(-\frac{(E - E_g)^2}{2\sigma_g^2}\right), \qquad (2.15)$$

where A_g, E_g and σ_g is the normalization, energy and width of the satellite peak, respectively. The resulting fit is seen in Fig. 2.11. We see that there is a small systematic error between the two peaks, which could be an effect of the satellite peak not having tails. However, the error from this is quite small and will be neglected.

We can deduce the thickness of the aluminum grid from the difference in energy between the two peaks. For U2, we have $E_0 - E_g = (147 \pm 2)$ keV which

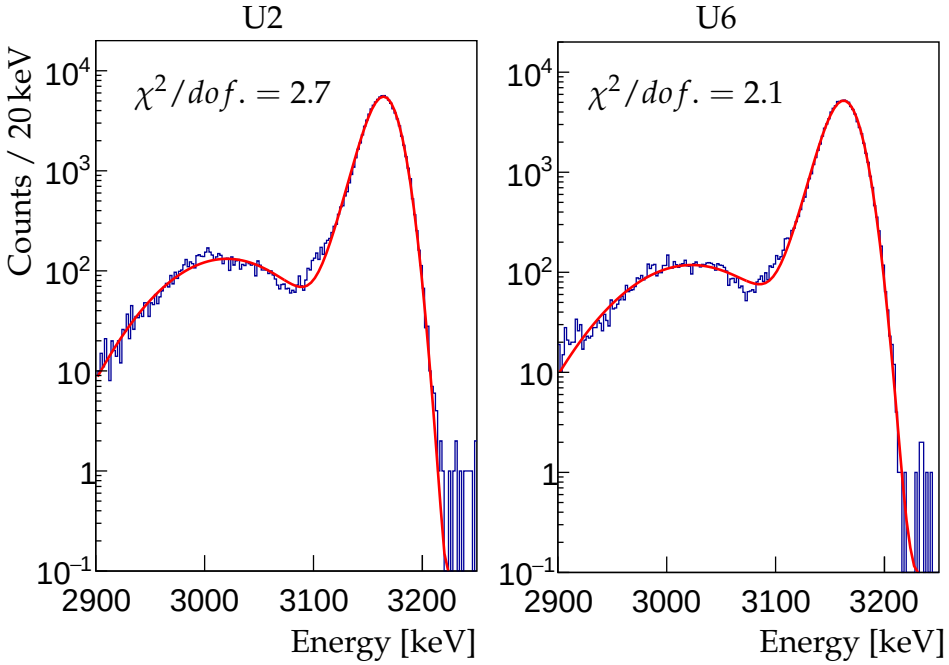

Figure 2.11: Fit to calibration peak in ^{148}Gd. The fitted response function takes into account the most prominent features of the detector response. There is a small systematic error in the area between the main peak and the satellite peak.

corresponds to a thickness of (0.66 ± 0.03) µm, and for U6 we have $E_0 - E_g = (151 \pm 2)$ keV which corresponds to a thickness of (0.68 ± 0.03) µm.

When analyzing the coincidence spectrum, it is important to know the detector response's effect on excitation spectrum. This can be found by folding the single-α response function from each detector as:

$$\Psi_{2\alpha}(E) = \int \Psi_1(E')\Psi_2(E - E')dE'. \tag{2.16}$$

The resulting coincidence response has four main contributions. The first comes from two α's hitting the aluminum grid, which is around $3\% \cdot 3\% = 0.09\%$ of the events and is therefore very unlikely. The next two comes from one α hitting the aluminum grid in one detector while the other does not. Because the deviations in the response function for each detector are quite small, it is difficult to differentiate one α hitting the aluminum in one detector versus the other, and therefore we actually see these two contributions as one. Lastly we have the main component, which is neither α hitting the aluminum and this corresponds to $97\% \cdot 97\% = 94\%$ of the events. The true coincidence response function for

U2 and U6 is seen as the blue lines in Fig. 2.12. This distribution was found by drawing a random hit for each detector, from the same peak and adding the energy. To simplify the expression for the coincidence response function Eq. (2.16) will not be used, instead we use the following parametrization:

$$\Psi'_{2\alpha}(E_0, E) = \Psi(E_0, E) + \psi_s(E_0, E), \tag{2.17}$$

where

$$\psi_s(E_0, E) = \frac{A_s}{\lambda_s} \exp\left(\frac{E - E_0}{2\lambda_s} + \frac{\sigma_s^2}{2\lambda_s^2}\right) \cdot \operatorname{erfc}\left(\frac{E - E_0 + \sigma_s^2/\lambda_s}{\sqrt{2}\sigma_s}\right). \tag{2.18}$$

The subscript s stand for "single", because this is single-tail version of Eq. (2.14). Equation (2.17) has three terms. The first is a dual tail Gaussian which is used to describe the main peak. The second is a simple Gaussian for the smallest peak, and the last term is the single tailed Gaussian for the middle peak. The resulting fit shows a small deviation at higher energies, but it is a extremely small correction and will be neglected. The coincidence response function broadens the measured distribution and shifts the peak energy down by $\sim$22 keV, which will be taken into account in the R-matrix analysis in Chapter 4.

2.7 Uncertainty estimation

We identify three sources of systematic uncertainties in the determination of the excitation energy spectrum, E_x. The excitation energy is determined as $E_x = E\alpha, 1 + E_{\alpha,2} - 92\,\text{keV}$, where E_{α_i} is the energy measured in one detector. For details on the calculations of E_x, see Section 3.1. The three sources of uncertainties are the following:

(1) Uncertainty in the calibration. The uncertainty of single α energy due to the linear fit in the calibration, is $\epsilon_2 = 2.5\,\text{keV} + 5.0 \times 10^{-4} \cdot E_\alpha$ for U2 and $\epsilon_6 = 2.1\,\text{keV} + 4.2 \times 10^{-4} \cdot E_\alpha$ for U6. This combines to a uncertainty of 5.2 keV at $E_x = 6.0\,\text{MeV}$ and 8.7 keV at $E_x = 16.0\,\text{MeV}$.

(2) Uncertainty in the energy-loss calculations. There are two contributions to the errors associated with energy-loss calculations. These are the precision of the calculations itself, and the precision of the distances used. For a discussion on the first contribution see [ZZB10]. In this estimate, we will assume these errors to be zero.

The errors on the energy-loss calculations due to uncertainties in the distances are again divided into two contributions, one for the detector dead-layer and one for carbon target thickness. The uncertainty on the carbon

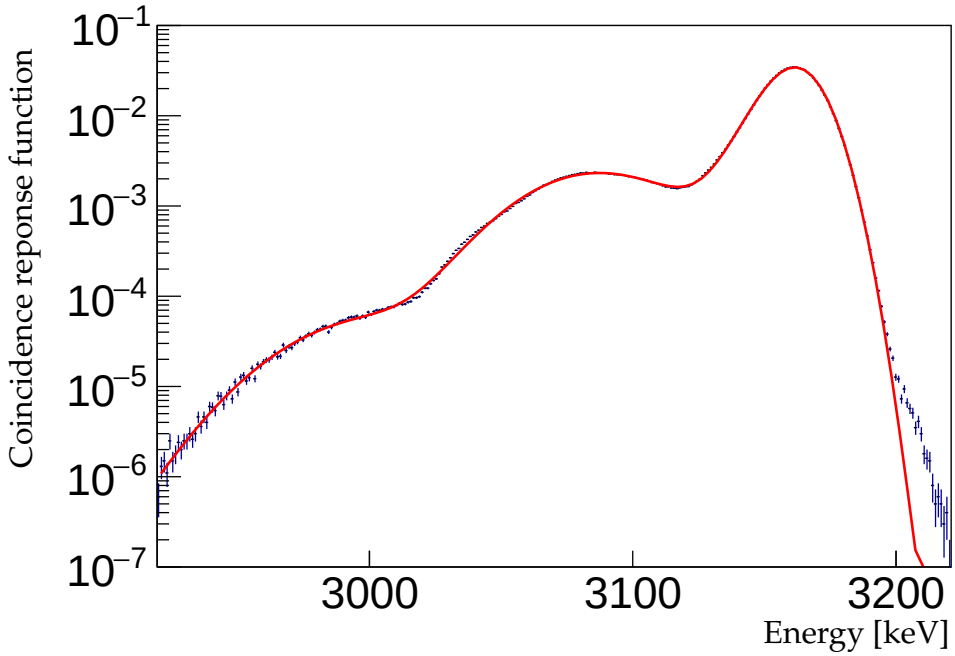

Figure 2.12: Coincidence response function, found by randomly drawing from the single-α response functions in U2 and U6. The red line is a fit to the form of Eq. (2.17).

target thickness and implantation depth found in Section 2.5.5, are 6 nm and 8 nm respectively. Energy-loss calculations show that this leads to a standard error of 1.5 keV and 2.1 keV for U2 and U6 respectively[5]. The combined error due to the energy loss in the foil is then 5 keV. A similar calculation done for the detector dead-layer, assuming 10% uncertainty in the dead-layer thickness, results in an uncertainty of 1.9 keV for a single α and 2.7 keV for the coincidence energy. These two effects lead to a total standard error on the coincidence energy of 5.7 keV.

(3) Uncertainty in determining energy due to detector response function. The coincidence response function found in Section 2.6, has a standard error on the peak energy of 3.4 keV.

The uncertainty from (1) is obviously energy dependent, while we assume the contributions from (2) and (3) are not.

[5]This is calculated assuming the particles travel with an angle of 90° to the plane of the foil.

By adding the contributions of (1)-(3) we get:

$$8.4\,\text{keV} \quad \text{at} \quad E_x = 6.0\,\text{MeV}, \tag{2.19}$$
$$10.9\,\text{keV} \quad \text{at} \quad E_x = 16.0\,\text{MeV}, \tag{2.20}$$

as a conservative estimate of the systematic uncertainty of E_x. This estimate seems reasonable, based on the results of the ^{226}Ra analysis in Section 2.5.4.

Chapter 3

Data Analysis and Results

In the previous chapter the experiment and the calibration was presented. This chapter will be concerned with the extraction and analysis of the excitation spectrum, E_x, and present experimental results. In Section 3.1 we will discuss the kinematics of the β-decay of ^{8}B and how to find the E_x spectrum. Sections 3.3, 3.5 and 3.6 will serve to present further analysis and validation of the E_x spectrum. Lastly, in Section 3.7, some initial results from the spectrum will be presented, and compared to the literature standard.

3.1 Determination of E_x spectrum

The β-decay of ^{8}B results in a recoil on the daughter nucleus (^{8}Be*), which then decays by $\alpha - \alpha$ breakup. Conservation of momentum leads to the two α-particles to be emitted exactly back-to-back with the same energy, in the rest-frame of ^{8}Be*. We can therefore write the velocity of the α's as $\vec{v}'_{\alpha,1} = -\vec{v}'_{\alpha,2}$. In the laboratory frame (rest frame of ^{8}B) we find the velocities by vector addition $\vec{v}_{\alpha,i} = \vec{v}'_{\alpha,i} + \vec{V}_R$, where $\vec{V}_R$ is the recoil velocity of the daughter nucleus. A schematic drawing of the two decays is seen in Fig. 3.1. The energy of the α particle can then be found

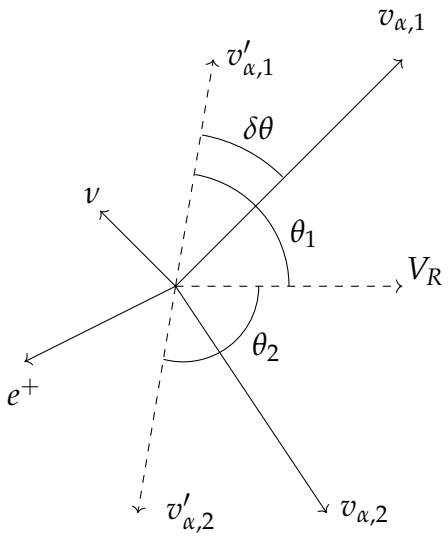

Figure 3.1: A 2-D schematic drawing of the β-delayed α-decay of ^{8}B.

as:

$$E_{\alpha,i} = \frac{1}{2} m_\alpha v_{\alpha,i}^2, \tag{3.1}$$

$$= \frac{1}{2} m_\alpha \left(v_{\alpha,i}'^2 + V_R^2 + 2\vec{v}'_{\alpha,i} \cdot \vec{V}_R \right), \tag{3.2}$$

$$= E'_\alpha + \frac{m_\alpha}{M_d} E_R + \sqrt{\frac{m_\alpha}{M_d} E'_\alpha E_R} \cos\theta_i, \tag{3.3}$$

where θ_i is the angle between $\vec{V}_R$ and $\vec{v}'_{\alpha,i}$, M_d and m_α are the masses of the daughter nucleus and α respectively, E_R is the recoil energy of the daughter nucleus and $E'_\alpha = E'_{\alpha,1} = E'_{\alpha,2}$ is the kinetic energy of the α particle in the rest frame of ^{8}Be*. When we measure the single-α-spectrum, we see a broadened and shifted spectrum due to the recoil from the β-decay. The last term in Eq. (3.3) vanishes when measuring coincidences because $\cos\theta_1 = -\cos\theta_2$. This lepton broadening effect will be investigated in more detail in Section 3.3.

Figure 3.2 shows the single and coincidence spectra zoomed in on the doublet levels. Here we see the effect of removing the recoil broadening, which allows us to more effectively differentiate the two 2^+ doublet levels.

In the case of ^{8}Be where $M_d = 2m_\alpha$, we can determine the excitation energy as:

$$E_x = 2E'_\alpha - 92\,\text{keV}, \tag{3.4}$$

$$= E_{\alpha,1} + E_{\alpha,2} + E_R - 92\,\text{keV}, \tag{3.5}$$

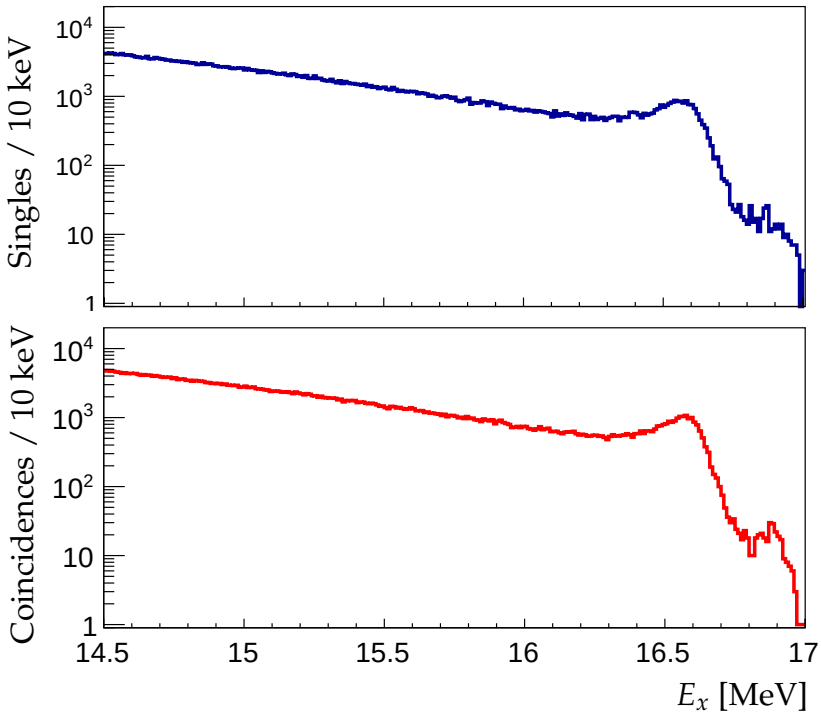

Figure 3.2: Comparison of the resolution for single events versus coincidences. The energy of the single events is calculated as $E_x = 2E_\alpha - 92\,\text{keV}$, while Eq. (3.5) is used for the coincidences.

where 92 keV is the energy difference between the ^{8}Be ground state and two unbound α particles. The size of E_R depends on the angle between the outgoing leptons, and will be maximum when they go out in the same direction. We can then estimate the maximum possible recoil energy from conservation of momentum as:

$$E_{R,max} = \frac{(E_0 - E_x)^2}{2M_d c^2}, \tag{3.6}$$

where $E_0 = 17.9798\,\text{MeV} - 511\,\text{keV} = 17.4688\,\text{MeV}$ is the maximum possible kinetic energy of the leptons, corresponding to a decay to the ^{8}Be ground state. The recoil energy for a decay to $E_x = 6\,\text{MeV}$ can be calculated as 8.8 keV and 0.05 keV at $E_x = 16.6\,\text{MeV}$. By measuring the energy and outgoing direction of the positron, one can make first order corrections to E_R. This is possible to do with the current detector setup, but it takes careful analysis to identify the positron, and will decrease the amount of statistics because the detection

efficiency is less than 100%. However, for the energy region we are concerned with, this is a negligible correction, and we will not concern ourselves further with this.

3.2 Data reduction

The data was analyzed using the Analyzer program in AUSAlib. The signal of interest is coincidence events of two α particles, with a sum energy of above 6 MeV. Because the BF_2 beam is very clean, the primary source of noise in this spectrum stems from positrons coming from the β-decay, which deposit less than 50 keV [PVG86] in the DSSD detectors. We therefore assume all particles in the energy range of interest, are α particles. Events with multiplicity one or larger in both detectors U2 and U6 are selected and the particles are then corrected for energy loss in the carbon target and detector dead-layer, assuming they are α particles.

Due to the lepton recoil effect discussed in Section 3.3, we are susceptible to false coincidences on the outermost strips. This effect is shown in Section 3.4 to cause angular shifts of up to $\approx 5^\circ$. This corresponds approximately to the angular width of one strip. To reduce the false coincidences, a condition is set that at least one of the particles has to have hit within the innermost 14×14 strips. Lastly the excitation energy is determined from Eq. (3.5) assuming $E_R = 0$.

3.3 Lepton broadening

When measuring the coincidence spectrum, the third term in Eq. (3.3) cancels out, as pointed out previously. However, we do see a significant broadening effect on the single α-spectrum due to this effect, which was seen in Fig. 3.2. The size and shape of the broadening is described in [BA02] for the specific case of β-decay from ^{8}Li and ^{8}B. The shape of the broadening can be described as:

$$\frac{dN}{dE}(x) = \begin{cases} \frac{15}{16T_{max}}(1 - 2x^2 + x^4) & -1 \leq x \leq 1 \\ 0 & \text{otherwise} \end{cases}, \tag{3.7}$$

with

$$T_{max}(E_x) = \sqrt{W_0^2 - 1}\frac{m_e}{M}\sqrt{2Qm_\alpha c^2 \frac{M - m_\alpha - Q}{M - Q}} \tag{3.8}$$

where T_{max} is the maximum recoil shift, $x = \delta E / T_{max} = \frac{1}{2}(E_{\alpha,1} - E_{\alpha,2})/T_{max}$ is the relative shift with respect to T_{max}, and m_e, m_α and M are the electron, α

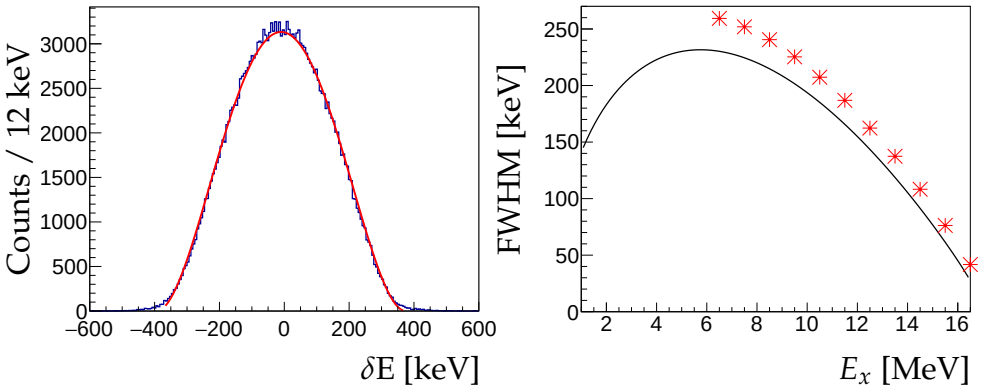

Figure 3.3: (Left) The difference in energy between the two α particles in coincidence events with $8\,\text{MeV} \leq E_x \leq 9\,\text{MeV}$. The red line is a fit to Eq. (3.7). **(Right)** Red stars are the measured FWHM, obtained through a fit, for excitation energies in intervals of 1 MeV. The blue line is the theoretical FWHM from Eq. (3.7).

and ^{8}Be masses, respectively. $W_0 = (E_0 - E_x)/m_e$ is the β endpoint in electron masses and $Q = E_x + 92\,\text{keV}$. The full-width-half-maximum (FWHM) of Eq. (3.7) is given as:

$$\text{FWHM}(E_x) = 2T_{max}(1 - 1/\sqrt{2})^{1/2} \simeq 1.082 \cdot T_{max}. \tag{3.9}$$

To analyze the broadening as a function of E_x, all events in the coincidence spectrum is divided into histograms for every 1 MeV and fitted to Eq. (3.7). Figure 3.3 (left) shows one of these fit and the red stars in Fig. 3.3 (right) shows the extracted FWHM as a function of E_x. The black line is the theoretical value extracted from Eq. (3.8).

Here we see that the measured broadening follows the same tendency as expected. It is clear however, that the observed FWHM is systematically larger than the theoretical value. There is an obvious explanation for at least some of this deviation. The effect of the detector response function has not been included in this analysis. To do this analysis correct, one would have to use Eq. (3.7) folded with the response function from Eq. (2.17) to fit the observed broadening. This would decrease the measured FWHM due to recoil, but it was unfortunately not possible to do within the time frame of this study. However, if we estimate the main part of the response function with a simple Gaussian, it has $\text{FWHM}_{\text{resp}} = 23.5\,\text{keV}$. By adding the FWHM of the theoretical broadening and response function in quadrature, we get an estimate for the expected measured broadening. This is of course a conservative estimate of the response functions impact, as it does not include the broad low-energy tail.

When including the estimated effect of the response function, the differences between the measured and theoretical FWHM are lowered. As seen in Fig. 3.3, the differences are larger for low E_x. The response function therefore also has a larger effect for large E_x. For $E_x \geq 13\,\text{MeV}$, the response function accounts for more than half of the difference. However, there is still a quite large energy-dependent contributions which is not explained. The reason for this is not known, but it could indicate that the data reduction has not eliminated all false coincidences.

3.4 Angular broadening

The lepton recoil does not only have an effect on the measured single α-spectrum. The recoil also makes it such that the α particles do not travel in completely opposite directions, as seen in Fig. 3.1. The magnitude of the angular shift depends on the outgoing angle of the α's in the rest frame of ^{8}Be*, and is largest when $\theta_1 = \theta_2 = 90^\circ$. In this case we find the relative angle between the two outgoing α's to be:

$$\Delta\theta_{max}(E_x) = 180^\circ - 2 \cdot \delta\theta, \tag{3.10}$$

where

$$\delta\theta = \arctan \frac{V_R}{v'_{\alpha,1}}, \tag{3.11}$$

$$= \arctan \sqrt{\frac{m_\alpha E_{R,max}}{M_d E'_\alpha}}. \tag{3.12}$$

This angle corresponds to the two leptons going out in the same direction and the two α's going out perpendicular to the the recoil motion. For $E_x = 16.6\,\text{MeV}$ the relative outgoing angle is $\Delta\theta \simeq 179.8^\circ$, so the angular shift at the doublet levels is almost zero. At $E_x = 6.0\,\text{MeV}$ the maximum shift is 175.6°. These examples were the maximum shift for a single event. When looking at the angular spectrum we expect to see a narrow distribution between 180° and $\Delta\theta_{max}$ for a given excitation energy. This distribution is simulated and shown in fig. 3.9 in [Kir10] for two different excitation energies.

Experimental effects can also lead to a broadening of the angular distribution. Four sources of uncertainty on the relative outgoing angles can be identified:

(1) Uncertainty of where the α particles hit on each pixel. Each pixel is $3\,\text{mm} \times 3\,\text{mm}$. In the analysis each event is given a random uniformly drawn position in the pixel. The maximum possible error on the position is

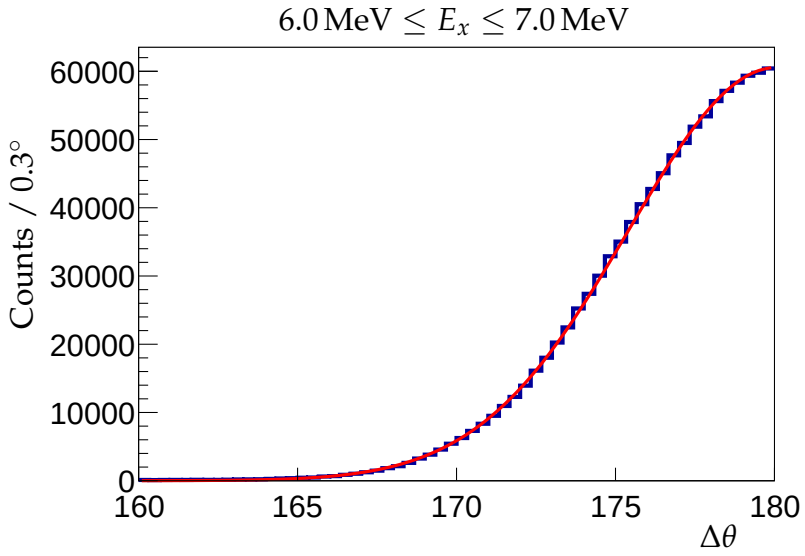

Figure 3.4: This plot shows the relative outgoing angle of the α's in coincidence events. The red line is a Gaussian fit with mean $\mu = 180.2°$ and standard deviation $\sigma = 4.7°$.

therefore $\sqrt{2} \cdot 3\,\text{mm} = 4.2\,\text{mm}$. The distance from the assumed implantation position in the target and the center of each detector is 34.5 mm for U2 and 37.8 mm for U6 during the ^{8}B run. If we assume the detectors to face the target squarely, then this leads to a maximum error of 6.9° and 6.3° for detectors U2 and U6, respectively.

(2) Uncertainty of the implantation spot of ^{8}B in the carbon target. There are actually two sources that contribute to this error. The first is the uncertainty due to different stopping lengths in the target. This has been simulated in TRIM and is conservatively found to be on the order of 10 nm, which is negligible. The other and more significant contribution is due to the beam of BF_2 not being completely collimated. Four collimators were used with the smallest being 4 mm. An error of 4 mm on the position of the decay, will lead to an error of the outgoing angle of approximately the same size as (1).

(3) General uncertainties from the geometry calibration of ∼0.1 mm on all positions. This effect is partly taken into account through (1) and (2), and is of negligible size compared to the others.

(4) Scattering of the α particles when going through the target and detector deadlayer. This effect has two components, the first being electronic scat-

tering and the second is nuclear scattering. The scattering in the deadlayer happens in the detector, and will therefore not have any significant impact.

Scattering in the carbon target will mostly only have an effect on the particles measured in U2, because the implantation depth is only $\sim$18 nm. Simulations in TRIM show that traveling through 110 nm carbon, will create a broadening of the angular distribution of up to 3° for an α particle. A few particles will experience significantly larger scattering due to nuclear collisions with a high impact parameter.

To summarize, we have three different sources of angular broadening due to geometrical uncertainties and one due to scattering processes. The contributions from (3) and (4) are much smaller than those from (1) and (2), and the experimental broadening effects are estimated to be significantly larger than the intrinsic recoil shift.

Figure 3.4 shows the angle between the two α's for coincidence events with $6\,\text{MeV} \leq E_x \leq 7\,\text{MeV}$. The red line is a Gaussian fit with mean of $180.83^\circ \pm 0.02^\circ$ and $\sigma = 4.66^\circ \pm 0.01^\circ$. The quality of the Gaussian fit indicates that the experimental broadening dominates the distribution over the intrinsic lepton broadening. However, we would still expect the Gaussian centered somewhere between 175.6° and 180°, which is not the case. The reason for this is not well understood.

3.5 Decay time

One of the variables saved for each event is the TPROTON described in Section 2.3, which is the time from the proton pulse was send until the event was triggered. From now on we will mention this trigger time as T_p. If the events we measure are indeed decays from the radioactive ^{8}B nuclei, then this time distribution should follow an exponential decay with the lifetime of ^{8}B[1]. However, the time distribution is not a perfect exponential decay, because the dead-time is larger right after a proton pulse which means a lesser fraction of the events are actually measured in this period. The T_p-spectrum can be seen in Fig. 3.5. At every 1.2 s there is a discontinuity due to the fact that the clock is reset every time we get a new proton pulse. The pulses does not come regularly, which means that sometimes there is 1.2 s between the pulses, sometimes 2.4 s and so on.

To analyze this spectrum we will use the Kolmogorov-Smirnov test (KS-test). This method tests a given distribution again the null-hypothesis or a so-called reference-distribution. The test works for arbitrary reference functions even including discontinuities. Another advantage is that this test works very well

[1] This is assuming the rate is low enough that only one decay is measured in each event

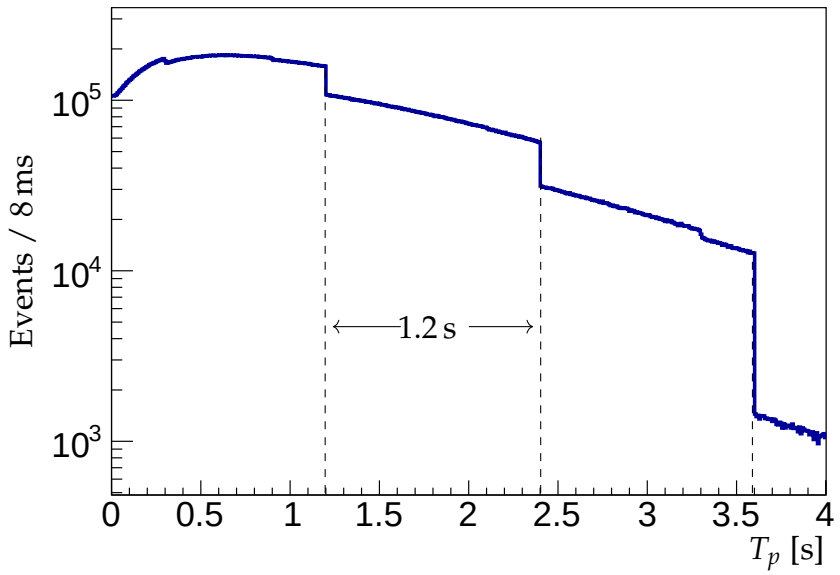

Figure 3.5: T_p-distribution of coincidence events. The discontinuities are due to the fact, that the proton pulses from the PS Booster are send out every 1.2 s and does not come regularly.

with small amounts of data. These are the primary reasons to use the KS-test instead of the more commonly used χ^2 test.

The goodness-of-fit is defined by the test statistic:

$$D = \max_{1 \leq i \leq N} \left(F(Y_i) - \frac{i-1}{N}, \frac{i}{N} - F(Y_i) \right), \tag{3.13}$$

where F is the reference distribution, Y are the ordered data points we test for, N is the number of data points, and i/N is the cumulative probability at data point number i. The test assumes that the data points are sorted and we know the exact value for each point. The KS-test should therefore generally not be used for binned data. We will be using ROOT's own implementation of the test, and the error associated with binned data is discussed in the ROOT documentation[2]. They have come to the conclusion that as long as the bin widths are much smaller than any physical phenomena of interest, the significance level (α) returned by the function should be approximately correct. The effect of using binned data (if any) is always to make α larger. Therefore we will be susceptible to accepting tests that might otherwise be rejected.

[2]The documentation can be found at `https://root.cern.ch/doc/master/classTH1.html`

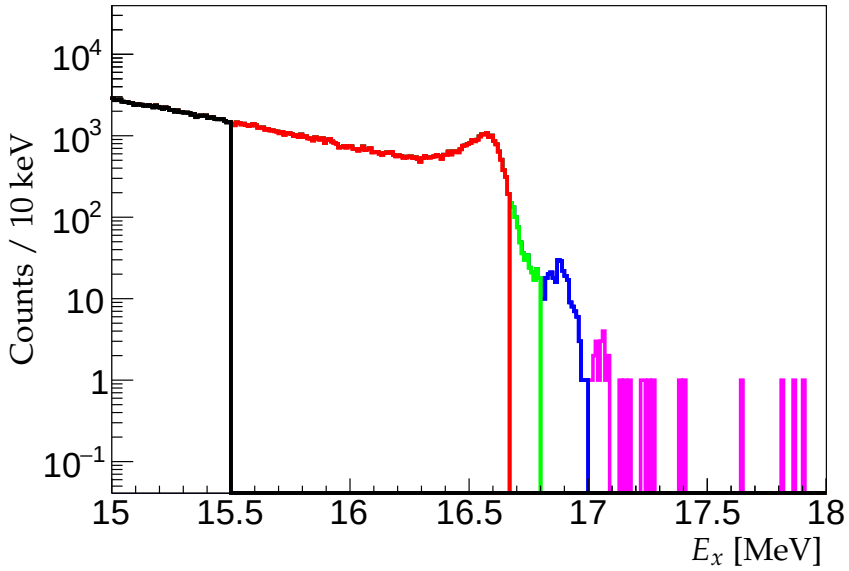

Figure 3.6: Coincidence spectrum zoomed in on the region around the 2^+ doublet. The color codings correspond to the regions in Table 3.1.

The null hypothesis is rejected with significance level α if:

$$D > c(\alpha)\sqrt{\frac{n+m}{nm}}, \tag{3.14}$$

where n and m are the number of counts in the reference and testing distributions respectively, and $c(\alpha)$ can be approximated as:

$$c(\alpha) = -\frac{1}{2}\ln(\frac{\alpha}{2}), \tag{3.15}$$

but is generally found in tables from literature.

The test is conducted on five T_p-distributions based on the E_x-spectrum. The region around the 2^+ doublet is of particular interest, as a small number of wrong coincidences can cause a significant error due to the low statistics in this region. The regions are shown divided by color in Fig. 3.6. The black area goes all the way down to 6 MeV and is the reference-distribution, while the red area signifies the 16.6 MeV level. The green is the intermediate region which is important in determining the interference between the levels. The blue region is the 16.9 MeV level and the purple are the events investigated in Section 3.6. The results from the KS-test are shown in Table 3.1.

Energy Region	α_0	α_1
15.50-16.67 MeV	0.199	0.329
16.67-16.80 MeV	0.459	0.028
16.80-17.00 MeV	0.872	0.891
17.00-18.00 MeV	0.958	0.687

Table 3.1: Table of results from KS-test on TProton-distributions with the reference distribution taken from 6.0 MeV $\leq E_x \leq$ 15.5 MeV. α_0 is the significance level for a test with all coincidence events. α_1 shows the same test, but including events where neither of the particles hit the innermost 14×14 strips.

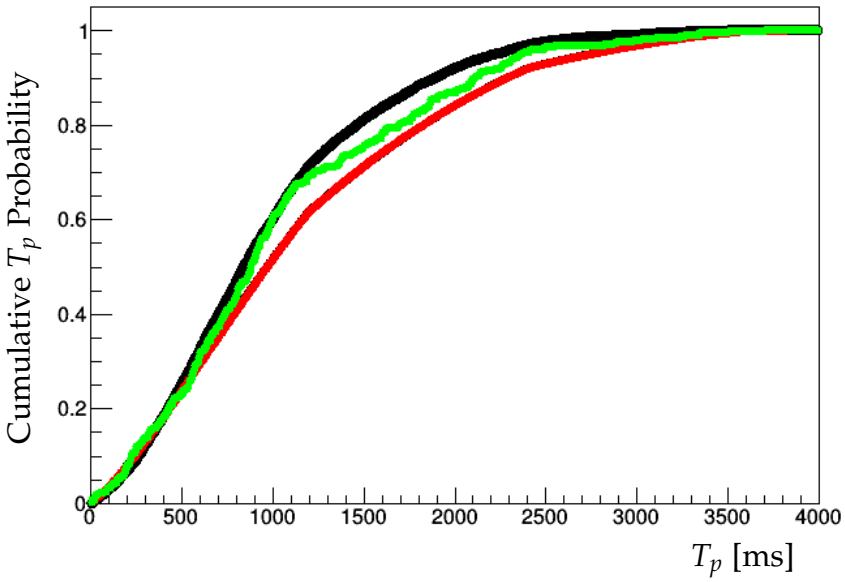

Figure 3.7: Plot of the cumulative T_p probability distribution. Red line is the standard reference distribution. The black line is the distribution for events with two physical events, corresponding to the square of the exponential decay distribution. The green line is the distribution for coincidence events with 16.67 MeV $\geq E_x \geq$ 16.80 MeV, without the demand that at least one α hits the innermost 14×14 pixels.

We deem the test of the null hypothesis true is the significance level is above 0.05. The middle column show the results for the coincidence reference distribution, where at least one of the particles hit within in innermost 14×14 strips. In this test, all regions has $\alpha \geq 5\%$, and none of them are close enough that the error associated with binned data plays a significant part.

For reference, the right column shows the results from a KS-test with the same reference-distribution, but with test-distributions including hits where none of the particles hit within the innermost 14×14 strips. In this case, one of the regions have a significance level below 0.05. When doing four tests with significance level of 5%, there is a $1 - 0.95^4 = 18.6\%$ chance of rejecting a true test, which means that this test is not significant in itself.

The red line in Fig. 3.7 shows the cumulative probability distribution for the standard reference distribution. The black line is a the distribution for events with two physical events, which means that it is the square of the single particle decay time distribution. The green line is the time distribution from the region between 16.67 MeV and 16.80 MeV, including events where neither α hits within the innermost 14×14 pixels. It is clear that the green line is somewhat of a combination between the red and black lines, which could indicate that there might be a significant part of false coincidences in this region. A similar plot excluding events in the outermost pixels, show that the distribution lies much closer to the red line, which is also why the KS-test was passed in this case.

As mentioned, the KS-test is not significant in itself, but leads us to the observation that the region between the 2^+ doublet levels might be more prone to false coincidences than the surrounding parts. This is important to be aware of, since this region is crucial in determining the exact interference between the levels. It seems, however, that the demand that at least one α hits within the inner 14×14 pixels reduce this effect. This analysis also suggests that the high rate of counts during the experiment, has led to a non-negligible amount of pile-up events which may be problematic across the entire spectrum. In general, as the events are uncorrelated, the spectrum does not on average change shape. However, in low statistics regions on the spectrum, it may cause an effect.

3.6 Analysis of high energy coincidences

In Fig. 3.2 there was an upper energy cut of 17 MeV. However, in Fig. 3.6, it is shown that the coincidence spectrum does have events at larger energies than 17 MeV. Here we see the 16.9 MeV level, which has a well defined upper edge at just below 17 MeV. There are then 31 events scattered around between 17 MeV and 18 MeV. These events has been investigated on an event-by-event basis, and a summary of this is what will be presented in this section.

We do not expect to see any events above the 16.9 MeV level and one way to explain these high energy events would be if two particles were summed as one. There are two possible scenarios for this. The first scenario is if the positron is emitted in the same direction as one of the α-particles and hit in the same pixel. The chance of this happening is $\sim 2 \cdot 9\,\mathrm{mm}^2/4\pi(3.5\,\mathrm{cm})^2 = 1.2 \cdot 10^{-3}$. We assume an average energy loss $0.4\,\mathrm{keV}\,\mu\mathrm{m}^{-1}$ for positrons in silicon [PVG86]. The energy deposited in the DSSD by a positron is then approximately $0.4\,\mathrm{keV}\,\mu\mathrm{m}^{-1} \times 60\,\mu\mathrm{m} = 21\,\mathrm{keV}$. The lowest energy events above 17 MeV are $\sim 100\,\mathrm{keV}$ above the upper limit of the 16.9 MeV level, which is too high for positron summing to explain it. Even if the energy was enough, there is only around 300 counts in the 16.9 MeV level. With the probability of $1.2 \cdot 10^{-3}$, we can estimate the number of events where this happens to around $300 \times 1.2 \cdot 10^{-3} = 0.4$. Again, this is clearly not enough to explain the 31 events.

The second possibility is for two α's to be detected as one. The initial pulse created by the α depositing energy in the detector is amplified in the Pre-amplifier to reduce noise in the measurement. The outgoing pulse from the Pre-amplifier has a sharp rise of $\sim 100\,\mathrm{ns}$, but a slow discharge of around $40 - 60\,\mu\mathrm{s}$, much longer than the length of an event. If another particle hits the same strip before the Pre-amplifier has discharged sufficiently, there is a possibility to count these two separate events as one, with an energy up to the sum of the two constituents.

If two α's were detected as one in one of the detectors, the difference in α energies, $\delta E = E_\alpha, 1 - E_{\alpha,2}$, would be on the order of MeV. However, none of these events has $\delta E \geq 300\,\mathrm{keV}$, so it seems unlikely that this is the case.

The last explanation is that two decays happened at the same time, resulting in the summing of α energies in both detectors. If the α's from one decay travel exactly back-to-back, the chance of α-summing in one detector is approximately the same as α-summing in both detectors. We saw in Fig. 3.4, that this is not the case. The angular width of one pixel is approximately $\arctan \frac{3\,\mathrm{mm}}{35\,\mathrm{mm}} \simeq 5^\circ$. To estimate the number of double summing events, we assume that if an α particle hits a pixel in one detector and $|\Delta\theta - 180^\circ| \leq 5^\circ/2$, then the other α can only hit in a single pixel in the other detector. So, the rate of double summing events (Γ_d) can be estimated from the total number of summing events (Γ), as:

$$\Gamma_d = \left(\frac{N(\Delta\theta \leq 180^\circ - 2.5^\circ)}{N} \right)^2 \times \Gamma, \tag{3.16}$$

where N is the number of total counts and $N(\Delta\theta \leq 180^\circ - 2.5^\circ)$ is the number of counts susceptible to double summing. This fraction is found from Fig. 3.4 to be $(56\%)^2 = 31\%$. Also, for two events to be summed as one, the time difference between them has to be small. We assume that two events that happen in the same pixel within 4 µs, will be summed.

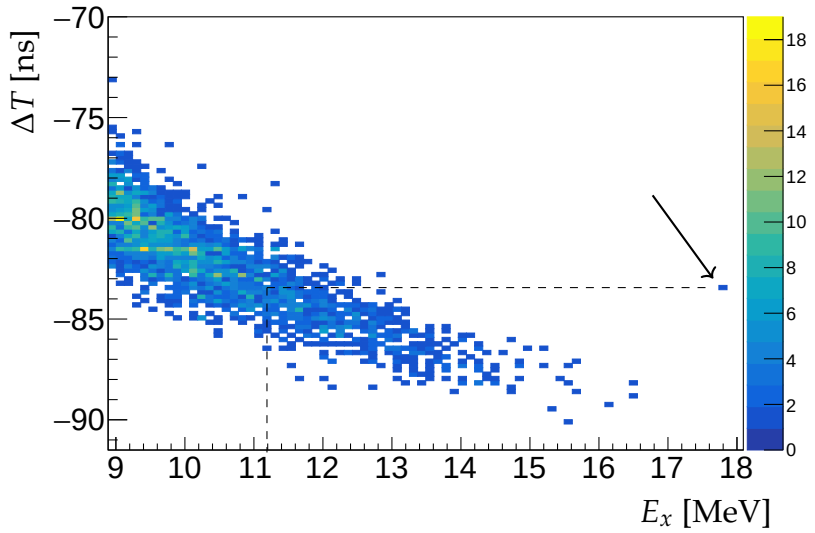

Figure 3.8: Plot of the time difference between events in U2 and U6. The arrow indicates the high energy event, that we believe are due to double α summing.

The rate of coincidence events varied throughout the experiment, but with an average rate of 362 Hz. With the solid angle of a pixel being 0.75%, the chance of summing is $\approx 0.75\% \times 362\,\text{Hz} \times 4\,\mu\text{s} \times (56\%)^2 = 3.4 \cdot 10^{-6}$, ie. 1 in every 300,000 events.

If we assume the "intruder" decay to come from the 3 MeV level, that means the original measured event has an energy between $11 - 12$ MeV. In the total spectrum there are $4.5 \cdot 10^6$ events in that energy range, which means we would see approximately 15 events of this type. Given that this is a very crude estimate, is it seems reasonable that it is off by a factor of two compared to the actual number of 31 events that we see.

There is another observation that supports this theory. Figure 3.8 shows the time difference between the signals in a single pixel U2 and U6, as a function of excitation energy. In general, one has to align each individual TDC channel, to be able to compare them. However, by including only one pixel from each detector, we achieve the best possible temporal resolution and avoid aligning all channels. The energy dependency stems from the fact that U2 uses a Leading Edge (LE) discriminator while U6 uses a Constant Fraction (CFD) discriminator. The LE discriminator has an energy dependence on the trigger time. This has been investigated by M. Munch from the Subatomic group at Aarhus University, and is shown to be in very good correspondence with what is seen in Fig. 3.8. The event highlighted by the arrow is one example of the high energy events. The

dashed lines show the expected E_x for an event with the same time difference as this particular event. That energy is found to be ≈11.2 MeV, which is in excellent agreement with the assumption that these events are due to double summing. This also explains why the cut above 17 MeV does not fail the test in Section 3.5, because the "intruder" decays have too low energy to trigger the detectors.

While there are a few of the events with $E_x \geq 17$ MeV that does not show this particular behavior, most of them do. The TDC analysis combined with the estimation on the number of counts, leads us to believe that this is in fact the right explanation and we will therefore exclude these events from further analysis. It also means that the spectrum below 17 MeV probably has double α summed events which has not been taken into account. However, this error is extremely small and the reason we see it in the high energy range, is because it is an otherwise empty spectrum.

3.7 Results

This section serves to present some initial results from the E_x spectrum extracted in the previous sections. This will be done mostly without the use of R-matrix theory. A more detailed R-matrix analysis of the spectrum is presented in the following chapter.

3.7.1 E_x spectrum

The final excitation spectrum is shown in Fig. 3.9 (left), with the right figure being the same spectrum, zoomed in on the region around the 2^+ doublet. One of the primary goals with the experiment IS633, was to measure the 16.922 MeV level. The only other time this level has been measured through β-decay, only five counts were seen in [Kir10]. The number of counts in the 16.922 MeV level in this study is found from Fig. 3.9 to be approximately 284, a factor of 57 more than the previous study. We can therefore conclude that the goal of measuring the 16.922 MeV with more statistics has clearly been achieved. For the first time, we have been able to measure 16.922 MeV level directly through β^+-decay, instead of inferring it from the low energy tails. This is of major advantage in the next chapter when doing R-matrix fits. With this amount of statistics, it is now possible to see if the fit is consistent with the data for that level specifically.

The present spectrum consists $1.21 \cdot 10^8$ coincidence events between 6 MeV and 17 MeV. For comparison, the number of counts in the entire spectrum in [Kir10] was 10.6×10^6. Using the normalization method described in Section 4.3, this corresponds to $1.30 \cdot 10^5$ events with 6 MeV $\leq E_x \leq$ 17 MeV. This results in a factor of 93 more in total statistics in this study, than any previous coincidence

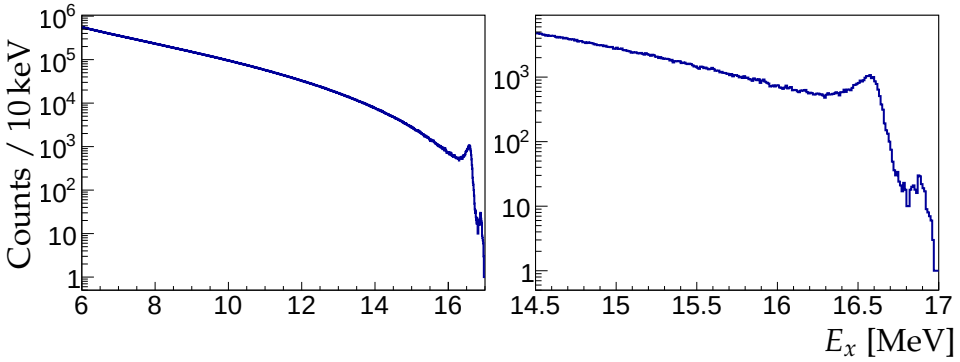

Figure 3.9: (Left) Final excitation spectrum of ^{8}Be based on coincidence events. The spectrum consists of $1.21 \cdot 10^8$ events. **(Right)** Excitation spectrum of ^{8}Be, zoomed in on the region around the 2^+ doublet. In this plot, the 16.922 MeV level is clearly seen.

analysis. As one may notice, this is not in perfect agreement with the fraction of counts in the 16.922 MeV level. This is most likely due to statistical fluctuations for the previous study, where a single count has a large impact.

The upper limit of the β^+-decay window for ^{8}B is situated only 36 keV above the 16.922 MeV level and 332 keV above the 16.626 MeV level. The phase space therefore skews the spectrum significantly, which is especially visible for the 16.626 MeV level, which is not very symmetric. The visible peak positions are also shifted down by the phase space factor [Rii+15], and it is therefore difficult to estimate the widths and positions of the levels on the basis of this spectrum. It is therefore not very meaningful to determine level parameters directly from the raw spectrum.

As mentioned in Section 1.2.3, the matrix elements for β^+ and EC are the same, and the total phase space be written as $f(E_x) = f_\beta(E_x) + f_{EC}(E_x)$. By assuming total isospin mixing between the 2^+ doublet levels, the matrix elements are equal for the two levels. This means that the ratio of counts can be estimated using only the phase space as:

$$r_{\beta+EC}(16.922/16.626) = \frac{f_{EC}(16.922) + f_\beta(16.922)}{f_{EC}(16.626) + f_\beta(16.626)} = 2.4 \cdot 10^{-2}, \tag{3.17}$$

where the energies are in MeV, and the phase space is calculated using Eq. (1.16) and the parametrization mentioned in Section 1.2.2. The number of counts in the 16.626 MeV level is not straightforward to find, because the peak does not have as well defined boundaries as the 16.922 MeV level. However, it is estimated that there are $\approx 1.6 \cdot 10^4$ counts in the 16.626 MeV peak, which gives a ratio of

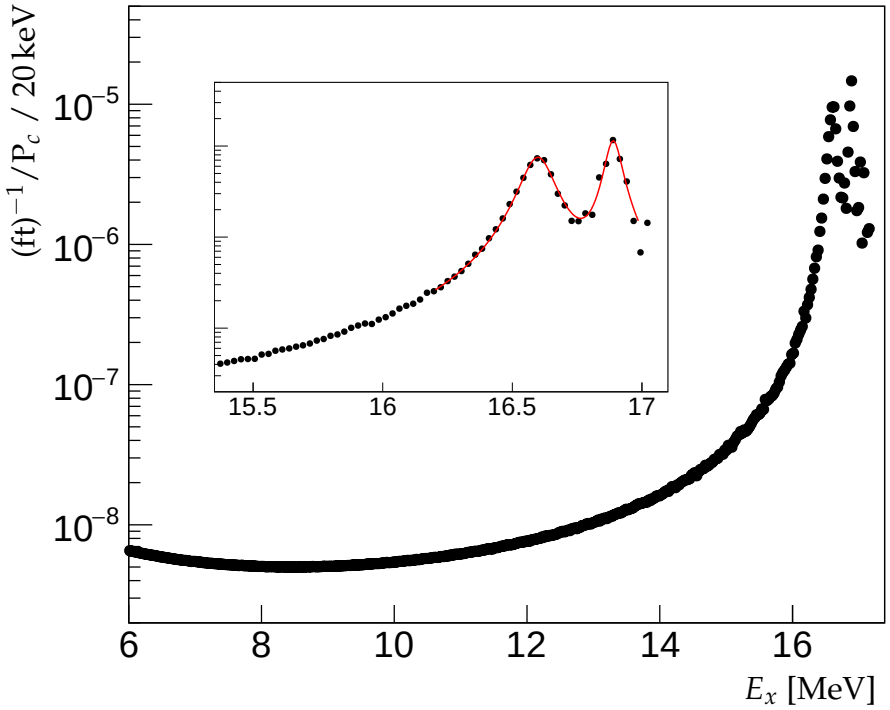

Figure 3.10: E_x spectrum converted into ft^{-1} and corrected for the $L = 2$ $\alpha - \alpha$ penetration factor. The figure in the middle is a zoom of the upper part of the larger spectrum. The red line is a two-level interfering Breit-Wigner fit, which is used to find the widths and positions of the 2^+ doublet levels. The fit results are seen in Table 3.2.

$1.8 \cdot 10^{-2}$. This is approximately 25% less than expected, but it does confirm the order of magnitude difference between the levels. The estimate is extremely dependent in the lower boundary of the 16.626 MeV level, and it is therefore not surprising that the result does not agree fully with the estimate. Also, the assumption that the levels are completely mixed in isospin is not correct, as the mixing coefficient is $\approx 59\%$.

3.7.2 Phase space corrected E_x spectrum

Figure 3.10 shows the measured E_x spectrum, plotted as the inverse ft-value and corrected for the $\alpha - \alpha$ penetration function. This plot gives a clear image of the pure ^{8}Be structure through β-decay, because kinematic factors for the entry channel and the energy dependency of the exit-channel have been removed. A similar

Parameter	Adopted levels	Fit	R-matrix fit
E_a [MeV]	16.626(3)	16.599(3)	16.619(1)
Γ_a [keV]	108.1(5)	131(9)	108(2)
E_b [MeV]	16.922(3)	16.889(2)	16.901(3)
Γ_b [keV]	74.04(4)	67(4)	65(3)

Table 3.2: Energy position and widths of the 2^+ doublet levels. Adopted levels are obtained from [Til+04]. The middle column are results from the Breit-Wigner fit seen in Fig. 3.10, while the right column are results from a simple R-matrix model with only two levels fitted to $E_x \geq 16\,\text{MeV}$.

plot has can be found in [Hyl10], with a coincidence energy threshold as low as 1.5 MeV. As we are limited to 6 MeV, it is not possible to show 3 MeV level in this plot. However, the high energy tail of this level is visible, and seen to dominate up to $E_x = 9\,\text{MeV}$. The maximum of the 3 MeV level is at approximately three orders of magnitude below the maximum of the doublet levels[3], and the width of the 3 MeV level found in [Til+04] is $\Gamma = (1.513 \pm 0.015)\,\text{MeV}$. The broadness of the level is not enough to explain the β strength in the intermediate region. Most of this strength can be explained by constructive interference between the levels, but it is known not to be enough. The last missing strength is the origin of Barker's proposed intruder state, but is now most widely believed to be due to the non-resonant direct decays discussed in Section 1.4.

The fit shown by a red line in Fig. 3.10, is two combined Breit-Wigner functions including interference. This fit is seen to explain the structure very close to the doublet quite well, and can be used to obtain the widths and positions of the 2^+ doublet levels. The result of this fit is shown in Table 3.2, along with the adopted levels from [Til+04]. The doublet levels are seen to interfere destructively in between the levels and constructively outside. To extract precise values, one would have to include the broadening of the coincidence response function found in Section 2.6, which is not included in the Breit-Wigner fit. However, this has been done with a simple R-matrix model, including only the 2^+ doublet levels for $E_x \geq 16\,\text{MeV}$. The result of this fit is shown in right column of Table 3.2. For an explanation on R-matrix theory see Chapter 4, but for now we just use results. The fit quality of the R-matrix fit is quite bad with $\chi^2/dof = 1.18$. This is to be expected since the model is too simple to describe all effects in the spectrum, as is shown in the next chapter. However, the fit is still valuable as a comparison

[3] Based on fig. 3.3 in [Hyl10].

with the fit results from Fig. 3.10.

When comparing the Breit-Wigner fit with the R-matrix fit, we see that the energies for both levels are lowered in the Breit-Wigner fit. The shift for the 16.6 MeV level is 8 keV larger than that of the 16.9 MeV level. A shift originating from the response function, would not necessarily shift the two levels equally, because the phase space changes to rapidly in this region. Γ_b is approximately equal in the two fit, while Γ_a is changed by 23 keV. Again, the response function does not necessarily have the same impact on the two levels due to the phase space. In fact, a R-matrix fit identical to the previous, but with no response function, confirms the parameters from the Breit-Wigner fit within the errors of the fit. This shows that one have to be careful when analyzing the detector response, as this can lead to significant errors in the resulting level parameters.

It seems very likely that the differences seen in the two fit, are well explained by the response function. This correspondence suggests internal consistency in the two models, when including the response function. However, even the R-matrix fit is not in very good agreement with the literature values for the doublet levels. The level energies for the 16.6 MeV and 16.9 MeV levels are 7 keV and 21 keV lower than the literature values respectively. The width obtained in the fit is equal to the literature value for the 16.6 MeV level and 9 keV too narrow for the 16.9 MeV level.

There are two possible explanations for this. The first is a systematic error in the spectrum. This has been investigated by adding an artificial energetic shift in the spectrum. However, several values for this shift has been examined, and none of them can be used to obtain literature values for both the energies and widths in the two-level fit. Generally a negative shift decreases the energies and broadens the levels, and vice versa for a positive shift.

A second explanation is the two-level fit itself. In the fit, contributions from all other levels in the spectrum are neglected. If this is not a valid approximation, this could lead to non-physical level parameters. However, a similar fit in Section 3.4.2 in [Hyl10], obtains very precise doublet level parameters, which are in agreement with the literature values within 3 keV.

The deviations in the fit parameters from the literature is most likely due to a combination of systematic errors in the calibration and the fit itself. As a result, the level parameters in the following R-matrix analysis can not be expected to produce precise results for the doublet levels. It can, however, still be useful in determining which models are best suited to describe the spectrum.

Chapter 4

R-Matrix Analysis

We saw in the previous chapter that the excitation spectrum measured from the β-decay of ^{8}B, exhibit broad features and the Breit-Wigner approximation is only able to describe the 2^+ doublet in a very local area. In this chapter we introduce R-Matrix theory, which is a framework for describing nuclear resonances in terms of physical meaningful parameters. In this chapter I will first give a brief introduction to the R-Matrix theory and discuss some of the possible limitations that we face with it. Next we will compare the excitation spectrum found in this study to a similar experiment conducted at the IGISOL facility of the Jyväskylä Accelerator Laboratory (JYFL) in 2008 and analyzed in [Kir10; Hyl10]. Lastly an alternative R-Matrix analysis is made specifically to the 2^+ doublet, in an attempt to extract physical parameters and the Gamow-Teller strength for the 2^+ doublet.

4.1 Theory

I this section, I will present a basic description of R-Matrix theory. For a complete description of the theory on the general many-channel, multi-level scattering process, I refer to the standard reference within the field [LT58] and the following reviews by [Vog62; Vog04]. For a generalization to β-decay followed by a two-body breakup, see [Bar69; Hyl10].

Let us first consider a nuclear decay $A \rightarrow B + C$. In general we can divide the interactions up in two parts, nuclear- and electromagnetic forces. Due to the short range of the nuclear force, electromagnetic interactions dominate on

large distances, while the nuclear forces are dominant on very short ranges. The essence of R-Matrix theory can then be boiled down to separating the configuration space into an internal and external part and matching the solutions at the interface. The size of the internal region is described by a bounding sphere with radius a_c, which we will call the channel radius. The size of this sphere is determined such that all nuclear interactions take place inside this region, and only Coulomb interaction is left in the external part. The short range of the nuclear force suggests that the channel radius should be only a few fm. In the external region, we are dealing with a two-body Coulomb problem. In this region one may write the wave function of a process with channels, c, as:

$$\Psi = \sum_c \psi_c u_c(r), \tag{4.1}$$

where ψ_c contains all spin and angular momentum dependencies and $u_c(r)$ is a solution to the radial Schrödinger equation. The solution to the radial part is a linear combination of an ingoing wave (I) and outgoing wave (O):

$$u_c = x_c O_c + y_c I_c. \tag{4.2}$$

The problem is now to determine the size and phase of the amplitudes, which can be described by the relation:

$$x_c = -\sum_c U_{c',c} y_c, \tag{4.3}$$

where U is the collision matrix. The ultimate goal is to know this collision matrix, as this is what describes the nuclear interaction. To do this, we need to know what happens in the internal region.

The internal region can be described by the Hamiltonian:

$$H = K + V, \tag{4.4}$$

where V is an unknown nuclear potential. As the exact form of V is not known, we cannot solve for the full wave function:

$$H\Psi = E\Psi. \tag{4.5}$$

However, we do know that there exists a complete basis of orthogonal eigenfunctions, X_λ, with eigenvalues, E_λ, from which the full wave function can be written:

$$\Psi = \sum_\lambda C_\lambda X_\lambda. \tag{4.6}$$

We then combine the two solutions by matching the logarithmic derivative of the wave functions at $r = a_c$. The next step is a long and demanding calculation, for which I will refer to [LT58]. In the end it turns out that the each internal eigenstate or level, λ, contributes to the collision matrix with two quantities, its energy, E_λ and reduced width amplitude, $\gamma_{\lambda,c}$. The subscript c indicates that each channel contributes with its own reduced width, and in this case there is only one outgoing channel, the 2α with $L = 2$, and two ingoing channels Fermi and Gamow-Teller β-decay. The inclusion of β-decay is described in [Hyl10], and instead of the reduced width it introduces the beta feeding parameter $g_{i,x}$ with $x = F, GT$, which can converted into the matrix element as:

$$M_{i,x} = \frac{g_{i,x}}{\left(1 + \sum_c \gamma_{i,c}^2 \frac{\delta S_c}{\delta E}\Big|_{E=E_i}\right)^{1/2}}, \tag{4.7}$$

where S_c is the shift-function, which is the real part of the logarithmic derivative of the outgoing wave O_c.

Since the collision matrix is not directly measurable, we need to convert this information into something measurable. In this study a decay spectrum is measured, which can be written in terms of the decay probability as $N(E) = (Nt_{1/2}/\ln 2)w(E)$, where $w(E)$ is the decay probability, N is the total number of decays in the whole spectrum and $t_{1/2} = (770 \pm 3)$ ms is the half-life of ^{8}B. The final expression for the spectrum is:

$$N(E) = \frac{Nt_{1/2}}{\pi B} f_\beta(Q - E) P_c(E) \left\{ \left| \sum_{i,j} \tilde{g}_{iF} \tilde{\gamma}_{jc} \tilde{A}_{ij} \right|^2 + \left| \sum_{i,j} \tilde{g}_{iGT} \tilde{\gamma}_{jc} \tilde{A}_{ij} \right|^2 \right\}, \tag{4.8}$$

where $B = (6147 \pm 2)$ s, f_β is the β-decay phase-space, P_c is the penetration function, i and j are the included levels, A is the level matrix which is connected to the collision matrix, γ is the reduced width of the outgoing channel, and finally g_x ($x = F, GT$) is the beta feeding parameter. We see from Eq. (4.8), that Fermi-contributions from all included levels interfere, and the same is true for the Gamow-Teller contributions. However, the Fermi and Gamow-Teller parts do not interfere with each other. The $\sim$ above g, λ and A in Eq. (4.8), indicates that we use a different parametrization than the standard. This parametrization provides observables directly from the fit and the derivation is found in [Hyl10; Bru02].

4.1.1 Comments on R-matrix theory

In the previous section, the internal and external wave functions where matched via their logarithmic derivatives at the surface of a sphere with channel radius,

a_c. In practice, one often determines the channel radius in terms of a nucleus independent constant r_0, as:

$$a_c = r_0(A_1^{1/3} + A_2^{1/3}), \tag{4.9}$$

where A_1 and A_2 are the mass number of the interacting nuclei. Previous studies has shown that there is often times a dependency of the observables from the fit on the channel radius. This effect is not necessarily a problem of the theory, but comes from the practical use of R-matrix theory.

In principle we have to include all possible levels in the R-matrix model to describe the internal interactions of two nuclei, which means including all internal basis-states. In practice the basis is truncated to a model with as few internal eigenstates (levels) as possible, while still producing a good fit to the data. This truncation corresponds to neglecting levels that are energetically far away from the measured spectrum. By increasing the channel radius, the contribution from the high-energy states becomes larger [Hyl10]. When using only the truncated basis, the level-parameters for the low lying states will change to compensate for this effect. To counter this, another level is often introduced which we will call the background level. This level should not be interpreted as a physical level, but more as a parametrization of the collective neglected effects that appears when using the truncated basis. If this background level is able to compensate for these effects, the remaining levels can be interpreted as physical levels and their parameters should therefore not change with varying channel radius. However, depending on the physical significance, the background level does vary in energy as a function of the channel radius. The background level discussed in the following sections is believed to signify the non-resonant contributions discussed in Section 1.4. For a more in-depth analysis of the background level, see chapter 5 in [Hyl10] and [Rii+15].

4.1.2 Isospin mixed doublet

The two states at 16.6 MeV and 16.9 MeV can be described as two isospin mixed states $|a\rangle$ and $|b\rangle$. These are linear combinations of two isospin eigenstates, $|T = 0\rangle$ and $|T = 1\rangle$, where the T= 1 state is the isobaric analogue state of the ^{8}Li and ^{8}B ground states. We can therefore write the two states as:

$$|a\rangle = \alpha\,|T = 0\rangle + \beta\,|T = 1\rangle, \tag{4.10}$$
$$|b\rangle = \alpha\,|T = 1\rangle - \beta\,|T = 0\rangle \tag{4.11}$$

with the condition $\alpha^2 + \beta^2 = 1$. The mixing coefficients, α and β, can be found by analyzing the observed widths of the doublet levels. α-decays with $\Delta T = 1$

are forbidden, and the observed widths are therefore $T = 0$ widths. This means that $\Gamma_0 = \Gamma_a + \Gamma_b$. Following the argument given in section 3.4.1 of [Hyl10], we can write the mixing coefficients as:

$$\alpha^2 = \frac{\Gamma_a}{\Gamma_a + \Gamma_b}, \tag{4.12}$$

$$\beta^2 = \frac{\Gamma_b}{\Gamma_a + \Gamma_b}. \tag{4.13}$$

The β-decay matrix elements for the doublet levels are a linear combination of the isospin eigenstate matrix elements:

$$M_{a,x} = \langle a|O_x|^8\mathrm{B}\rangle = \alpha M_{0,x} + \beta M_{1,x}, \tag{4.14}$$

$$M_{b,x} = \langle b|O_x|^8\mathrm{B}\rangle = \beta M_{0,x} - \alpha M_{1,x}, \tag{4.15}$$

where $|^8\mathrm{B}\rangle$ is the ground-state of ^{8}B. Because of isospin conservation in Fermi-decay, $M_{0,F} = 0$ and using Eq. (1.10): $M^2_{1,F} = T(T+1) - T_3(T_3+1) = 2$. Shell-model calculations predict that $M_{1,GT}$ is very small compared to $M_{0,GT}$ [War86b]. This results in the following equations:

$$M_{a,F} = \sqrt{2}\beta, \qquad M_{a,GT} = \alpha M_{0,GT} + \beta M_{1,GT}, \tag{4.16}$$

$$M_{b,F} = -\sqrt{2}\alpha, \qquad M_{b,GT} = \beta M_{0,GT} - \alpha M_{1,GT}. \tag{4.17}$$

The 2^+ doublet level parameters were determined by Hinterberger *et al.* [Hin+78] using elastic scattering of α particles. They analyzed the 16 MeV doublet using R-matrix theory in the single-channel, two level approximation without contributions from other 2^+ levels. The level parameters found directly from the fit, are therefore not the physical doublet parameters. However, it is possible to transform the fit parameters into physical level parameters via a non-trivial transformation. The way to do this is described in Section 3.4.1 in [Hyl10].

4.2 Details of the analysis

In the following R-matrix analysis, we will use the Open R-Matrix (ORM) program, developed by M. Munch, O.S. Kirsebom and J. Refsgaard in the AUSA-group [MKR18]. ORM provides a library for doing R-matrix calculations, and a command-line interface for performing fit to experimental data. The program is an implementation of the R-matrix theory as summarized by [LT58], and is able to handle $\beta-$ and γ-decays experiments. At the time when this analysis was started, the program was not yet complete for the case of β-decays. I have therefore personally contributed with several functionalities to the program,

both general and more specific to β-decay. These include, but are not limited to, the calculation of Fermi- and Gamow-Teller matrix elements, coupling included levels through Fermi- and Gamow-Teller decay channels, and added the possibility of locking fit parameters with respect to each other. The last functionality is still limited in the parameters that can be fixed, which in turn has limited the possibilities in this analysis.

Each level included in the truncated R-matrix basis, creates one fit parameter for each channel it couples to and one that determines the level energy. The α-channel parameter can be converted into the width of the level, while those for beta-decays can be translated into the matrix element fo the corresponding decay. The B_{GT} values listed in Tables 4.1 and 4.2 are corrected for the vector and axial-vector coupling constants as shown in Section 1.2.2, while $M_{a+b,GT}$ does include the factor $\frac{g_A}{g_V}$. The individual level contributions shown in each plot, are calculated using Eq. (4.8), with the sums including only one level.

The spectrum we see from the data, is affected in part by the detector response as discussed in Section 2.6. To account for this in the R-matrix function, the calculated spectrum is folded with the normalized coincidence-response function. The calculated spectrum we see in the fit, is therefore not a pure R-matrix spectrum, but includes experimental effects.

The fitting of experimental data is done through the Minuit program implemented in ROOT and described in [JR75]. The function used to minimize is a log-likelihood function:

$$\chi^2 = 2\sum_i \left(n_{i,\text{fit}} - n_{i,\text{data}} + n_{i,\text{data}} \ln\left(\frac{n_{i,\text{data}}}{n_{i,\text{fit}}}\right)\right), \tag{4.18}$$

where $n_{i,\text{data}}$ and $n_{i,\text{fit}}$ are the experimental and calculated values respectively. The standardized residuals shown below each fit are calculated as:

$$\delta_i = \frac{\left(n_{i,\text{fit}} - n_{i,\text{data}}\right)}{\sqrt{n_{i,\text{fit}}}}. \tag{4.19}$$

4.3 Comparison to previous experiment

In this section, we compare the new measurements from IS633 with previous R-matrix fits done to the same type of experiment. More specifically we consider the β-delayed α-spectrum from an experiment done at JYFL in 2008. This experiment and the analysis of it, is described in detail in [Kir10] and the following R-Matrix analysis is found in [Hyl10; Kir+11]. This reason to use this particular experiment, is because it has the most statistics of any previous experiments concerned with

β-decay of the ^{8}B ground-state. The data from JYFL 2008 will from now on be mentioned as JYFL08, while the data from this study is mentioned as IS633.

4.3.1 Normalization

The difference in statistics in the two experiments is shown in Fig. 4.1, and is roughly a factor of 853[1]. As one may notice, this factor is not the same as discussed in Section 3.7. As the data from JYFL08 is from 2008, some aspects of the data analysis has been lost. After talks with O.S. Kirsebom, who did the analysis back then, he advised to use the dataset seen in Fig. 4.1 (left). The data used for the R-matrix analysis in [Hyl10; Kir10], had roughly a factor of 10 more statistics. This is the reason that the five counts in the 16.922 MeV level is not seen in the present spectrum.

As a simple check to see whether the two spectra, JYFL08 and IS633, are consistent, a linear fit is made to the fraction of counts in each bin. This fit is shown as the red line in Fig. 4.1 where $\alpha = 853(6) + \mathrm{E_x} \cdot 0.7(5)/\mathrm{MeV}$. We see here that the fraction of counts in each bin is almost constant within the errors as a function of energy. If a small shift of one bin (20 keV) is made to the IS633 spectrum, then the fit becomes $\alpha = 854 - \mathrm{E_x} \cdot 0.4(5)/\mathrm{MeV}$, in which case the slope changes sign. The non-zero slope could indicate that there may be an energetic shift between the two spectra. A simple estimate of this shift is 0.4/0.7·20 keV=11 keV. This observation is in agreement with the estimated error in Section 2.7.

Equation (4.8) assumes that N is the total number of counts for the entire spectrum all the way down to zero energy. The beta-strength parameters $g_{i,x}$ therefore depends on the the number of counts as $1/\sqrt{N}$. Because we are not confident in our spectrum below 6 MeV, we have to ensure the normalization of the fit in some other way. To do this, the excitation spectrum from [Kir10] is used to get the fraction of counts between 0-17 MeV and 6-17 MeV. This factor is multiplied with the number of counts in the IS633 spectrum between 6-17 MeV. This way the assumed number of counts in our spectrum is:

$$N_{\mathrm{IS633}} = \frac{N_{\mathrm{JYFL08}}(0-17)}{N_{\mathrm{JYFL08}}(6-17)} \cdot N_{\mathrm{Is633}}(6-17), \tag{4.20}$$

where the numbers indicate the energy range in MeV. This method has been tested by integrating the final R-matrix fits down to $E_x = 0$, and is found to be equal within 1%.

[1] Based on the data above 6 MeV because of the low energy problems discussed in Section 2.5.6

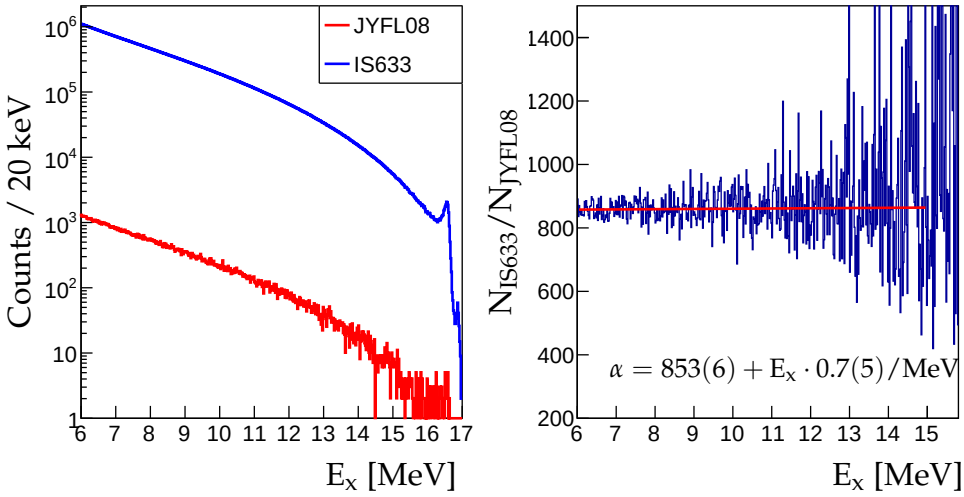

Figure 4.1: (Left) This plots shows the coincidence spectra obtained from JYFL08 (red) and IS633 (blue). **(Right)** The fraction of events for every 20 keV bins. The red line is a linear fit, shown in the lower part of the plot.

4.3.2 R-matrix fit

Because of the limitations of the data below 6 MeV, the JYFL08 spectrum from [Kir10; Hyl10] is included, as well as the IS633 data. The old spectrum has a lot of statistics at the main peak and goes down to 1.5 MeV. This way, the new data will dominate at 6 MeV and above, because there is so much more statistics. The old data set can then be used to determine the position and width of the main peak and will not influence the high-energy part of the spectrum significantly. The main peak is already well known, and is not of particular interest in this study, and it is therefore acceptable to use previous data for this part.

The truncated basis used in this analysis will consist of four 2^+ levels. The initial guesses for the energies of the first three levels are 3.03 MeV, 16.626 MeV, and 16.922 MeV. These levels are interpreted as physical levels, while the fourth acts as a background level.

In Model 2 of [Hyl10], the level parameters for the doublet are calculated on the basis of the isospin eigenstates, and the parameters are then converted into the physical doublet level parameters using the theory presented in Section 4.1.2. More specifically the mixing coefficients are calculated from Eq. (4.12) using literature values for the widths [Til+04]. The Fermi-strength parameters are calculated from Eqs. (4.16) and (4.17), and the Gamow-Teller strength for the $T = 1$ state is set to zero. The Fermi-strength for the 3 MeV- and background

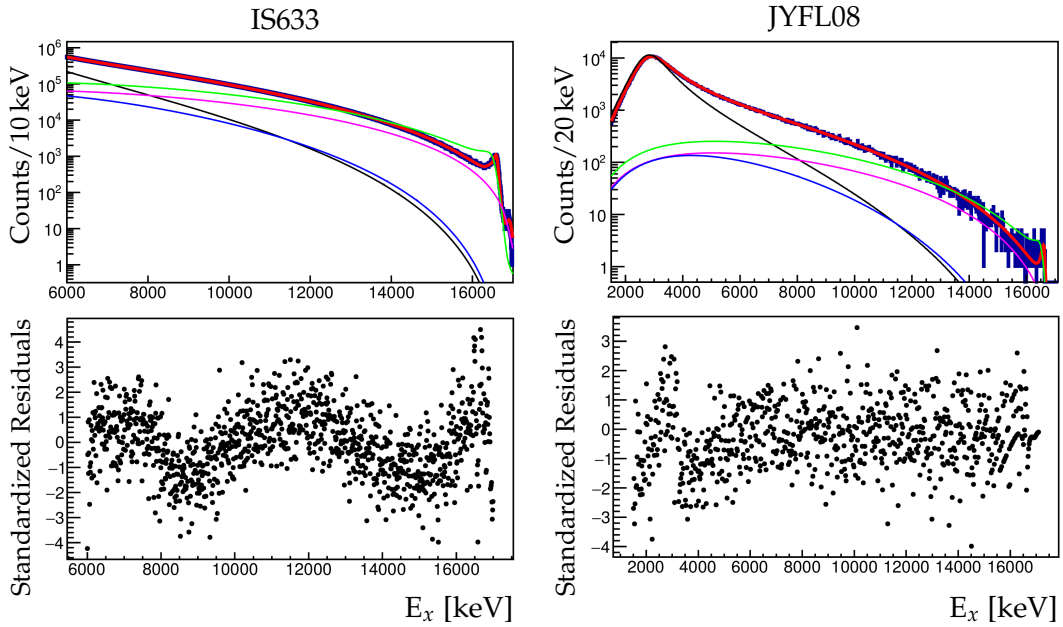

Figure 4.2: Combined R-matrix to data from JYFL08 (1.5 MeV $\leq E_x \leq$ 17 MeV) and IS633 (6 MeV $\leq E_x \leq$ 17 MeV). The black, green, purple and thin blue lines are the contributions from the 3 MeV, 16.6 MeV, 16.9 MeV and 37 MeV levels respectively. The thick blue line is the data and the red is the total R-matrix fit.

levels are also fixed to zero, because they are both predicted to be very small [Wir+13]. The energy of the background level was fixed to 37 MeV, while the width was scanned manually and an optimal solution was found for 126 MeV.

In this study, we have more statistics in the doublet area, which makes it possible to fit some of these variables instead. To compare with the results from Model 2 in [Hyl10], the same levels and channel radius are used. We also demand that the sum of Fermi matrix elements squared equal 2, but let the mixing coefficients be free variables. The Fermi-strengths for the 3 MeV and background levels are likewise fixed to zero, while the energy and width of the background level are fixed to the same values as in [Hyl10].

The resulting fit is seen in Fig. 4.2 and the corresponding fit parameters are shown in the right column of Table 4.1. The doublet levels are lower in energy and around 3 times wider, than the adopted levels from [Til+04] in the left column. This is not a problem in itself, because of the transformation into doublet parameters discussed in Section 4.1.2. Unfortunately, this transformation has not been made due to time constraints. This is an obvious next step in the analysis. However, the values from [Hyl10] has not been corrected either, so this comparison is still valid. The doublet level parameters found in this fit,

Parameter	Adopted Levels	JYFL08	IS633
r_0 (fm)		1.35	1.35
E_3 (MeV)	3.03(10)	3.054(5)	3076(2)
Γ_3 (MeV)	1.513(15)	1.47(2)	1.636(4)
$B_{3,GT}$		0.0102(2)	0.0107(5)
$M_{a+b,GT}$		1.84(2)	1.75(8)
E_a (MeV)	16.626(3)	16.544	16.547(2)
Γ_a (keV)	108.1(5)	355	325(8)
$B_{a,F}$			$1.46(3)^{\dagger}$
$B_{a,GT}$			0.70(2)
E_b (MeV)	16.922(3)	16.887	16.874(5)
Γ_b (keV)	74.0(4)	120	195(10)
$B_{b,F}$			$0.54^{\dagger}$
$B_{b,GT}$			1.21(8)
E_B (MeV)		37.0	37^{*}
Γ_B (MeV)		126(3)	126^{*}
$B_{B,GT}$		0.032(6)	0.034(1)
α_Γ^2	59%	74%	60%
$\chi^2/dof.$		0.97	1.58

Table 4.1: Fit parameters from R-matrix fits. All levels are 2^+ and the labeling is the following: 3 is the 3 MeV, a and b are the doublet levels and B is the background level. Left column are adopted levels from [Til+04], and the middle column shows the results from [Hyl10]. The right column shows results from the analysis based on data from IS633 and JYFL08. The mixing coefficient α_Γ is calculated using the doublet widths and Eq. (4.12). Parameters indicated with a * are fixed in the fit, and parameters with a † are fixed with respect to each other so they sum to 2.

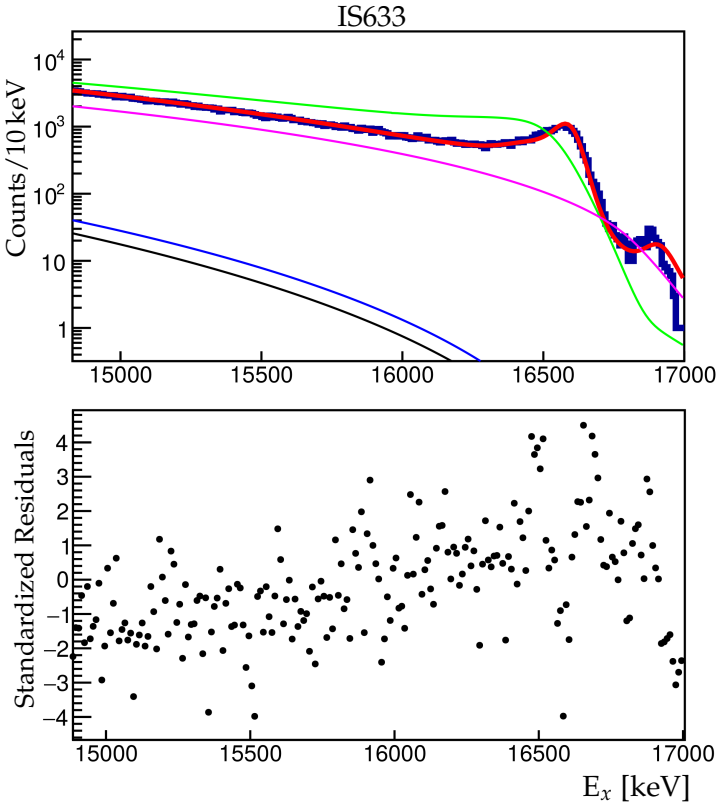

Figure 4.3: R-matrix fit to data from IS633 and JYFL08. The plot shows that IS633 data above 14 MeV. The black, green, purple and thin blue lines are the contributions from the 3 MeV, 16.6 MeV, 16.9 MeV and 37 MeV levels respectively. The thick blue line is the data and the red is the total R-matrix fit.

are in quite good agreement with the ones from [Hyl10] in the middle column. The energy positions are within a few keV for the doublet levels, and the total Gamow-Teller strength of the 2^+ doublet levels is barely equal within the errors. The widths of the doublet levels are not equal in the two fit, but they are both very large compared to the adopted widths. This leads us to believe that this model is mostly in agreement with the results found in [Hyl10].

Another thing worth noting, is the distribution of Fermi strength between the 2^+ doublet levels. In this fit most of the Fermi strength lies in the 16.6 MeV level, which is the opposite of what we expect based on the widths of the levels and Eqs. (4.16) and (4.17).

In the fit from [Hyl10] there is such little data in the doublet region, that it is difficult to see the structure of the doublet levels. However, if we zoom in on the high energy region on the new spectrum, something interesting appears in

Fig. 4.3. Neither of the doublet levels have the structure of a regular level, in the sense that they do not show a peak. Instead they both have a broad "shoulder", and the two resulting peaks are created from interference between the levels. This leads us to believe that the doublet levels obtained in this model are not physical levels, but instead they act merely as an effective parametrization of the high energy part of the spectrum.

With $\chi^2/dof. = 1.58$, this fit is significantly worse than the one made in [Hyl10]. This could in part be due to the effect of a small energetic shift between the two spectra. However, it seems unlikely to explain the large systematic errors on the IS633 residuals. More likely is it that due to the low statistics, the 16.9 MeV level in the JYFL08 data, was able to act partly as a secondary background level. Then the role of this level is not only to account for the actual 16.9 MeV level, but also to mask deficiencies of the model in the lower part of the spectrum. This would explain why the fit is so bad for the IS633 data, while describing the JYFL08 data nicely above 6 MeV. It also explains why the fit is not well centered around the visible peak at 16.9 MeV in the IS633 data. It therefore seems likely that the background level used in this model might not be suited to describe the non-resonant effects in the spectrum.

4.4 Fit to 2^+ doublet

The individual level contributions shown in Fig. 4.2, show that the 3 MeV level and the background level are approximately two orders of magnitude weaker than the doublet levels above 14 MeV. New fits are therefore made with a low-energy cut at 14 MeV, where only the 2^+ doublet levels and a background level is included. This means that the background level will have to account for the small contribution from the 3 MeV level, as well as the non-resonant contribution. Like in the previous fit, the sum of the doublet Fermi matrix elements squared, is set to 2 and the Fermi strength for the background level is fixed to zero. Four models have been fitted, with the energy and width of the background level fixed for each fit. The fit parameters for all four models are shown in Table 4.2. Each of model will briefly be discussed individually in Sections 4.4.1 to 4.4.4, and a discussion of all four models will be given in Section 4.4.5.

4.4.1 Model 1

The first model to consider, is approximately the same as in the previous section. The background level is at 37.0 MeV with a width of 126 MeV. The fit is shown in Fig. 4.4, where the color scheme is the same as in Fig. 4.2. Comparing with Fig. 4.3, the residuals are more evenly distributed around zero with little systematic

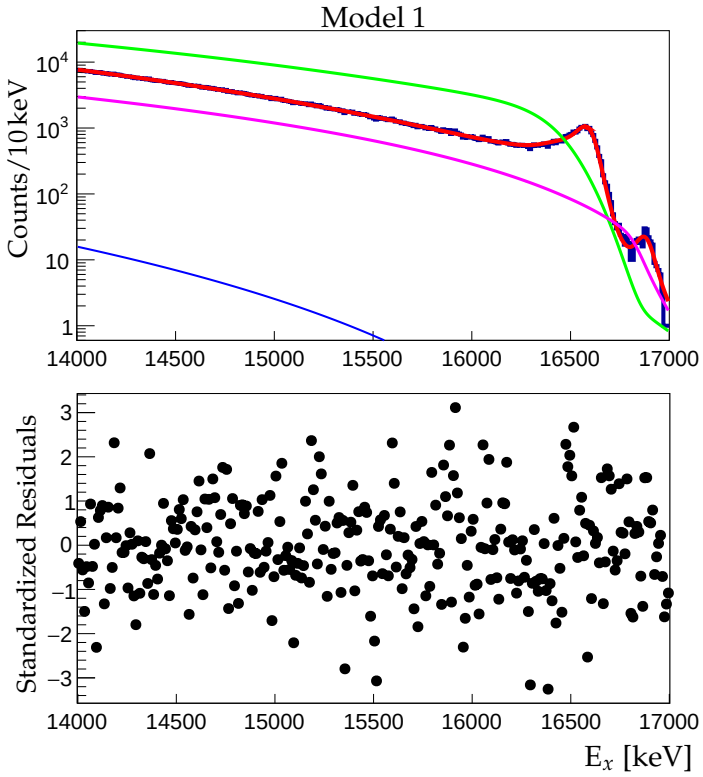

Figure 4.4: R-matrix fit of model 1 to data from IS633 above 14 MeV. The green, purple and thin blue lines are the contributions from the 16.6 MeV, 16.9 MeV and 37 MeV levels respectively. The thick blue line is the data and the red is the total R-matrix fit.

deviation. With $\chi^2/dof. = 1.05$, the fit is generally better, which is not surprising, given that the model has to describe a smaller region. The Fermi strength is switched between the levels compared to the fit in Fig. 4.2, with the 16.9 MeV level now having the largest part. This is in agreement with the literature. The mixing coefficient α^2_{BF} is too large, but the large errors on $B_{a,F}$, due to very large correlations, could explain this. The doublet Gamow-Teller strength is equal to that from the previous fit.

Visually it is clear that the position of the 16.9 MeV level and the immediate area around 16.6 MeV is better described in the present fit than in Fig. 4.3. However, the individual levels are still broad with no peak-like structure, which suggests that a very broad background level at 37 MeV does not give a physical description of the region around the 2^+ doublet levels.

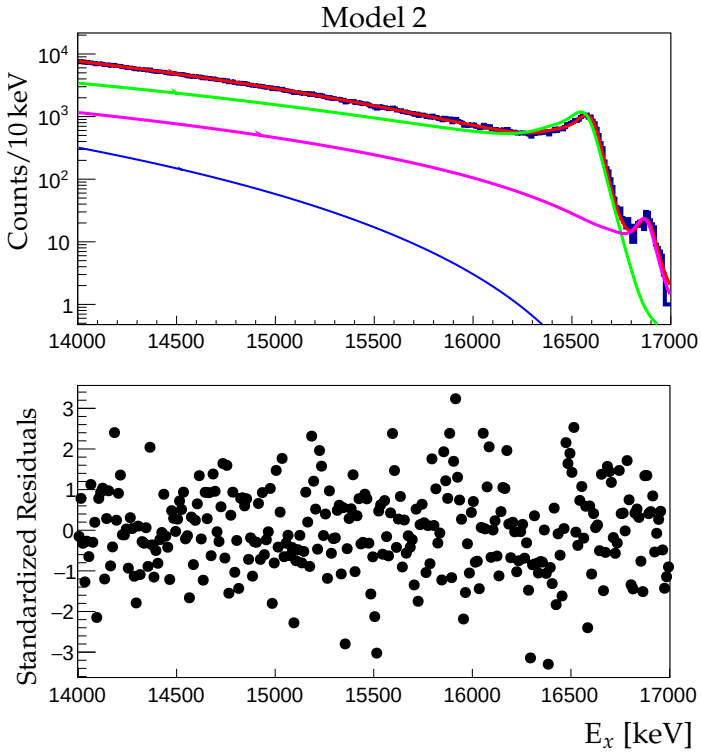

Figure 4.5: R-matrix fit of model 2 to data from IS633 above 14 MeV. The green, purple and thin blue lines are the contributions from the 16.6 MeV, 16.9 MeV and 37 MeV levels respectively. The thick blue line is the data and the red is the total R-matrix fit.

4.4.2 Model 2

The background level used in Model 1 is extremely broad, resulting in an approximately constant background contribution. For a narrow background level, the contribution gains an energy dependency. In Model 2 the background level is still fixed at 37 MeV, but the width is changed to 24 MeV to add more structure to the background level. A fit to this model is shown in Fig. 4.5.

The residuals in this plot do not show any significant systematic error, and with $\chi^2/dof. = 1.04$, the fit quality is a bit better than that of the fit to model 1. The individual contributions of the 2^+ doublet levels show a clear peak structure that was missing in the previous model. The resulting fit parameters for the 2^+ doublet levels in this fit, are more similar to the values found in Section 3.7.2.

Both of the level energies are still too low for both levels, and Γ_a is too large. Γ_b is now too narrow compared the literature values, but is in agreement with that of Section 3.7.2. The contribution from the background level is approximately 25

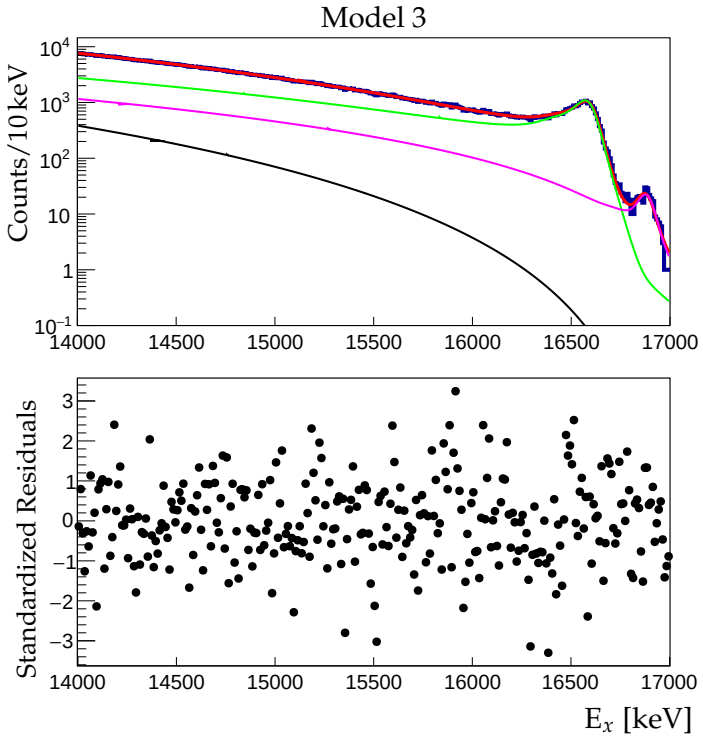

Figure 4.6: R-matrix fit of model 3 to data from IS633 above 14 MeV. The green, purple and thin blue lines are the contributions from the 16.6 MeV, 16.9 MeV and 37 MeV levels respectively. The thick blue line is the data and the red is the total R-matrix fit.

times greater than in model 1. This is not surprising since the width of this level is much smaller, which means that the strength has to be larger, to get a similar total background contribution around 16 MeV.

The mixing coefficient based on the widths and Fermi strength are both reduced compared to model 1, and the one based on the Fermi strength, is now equal to the expected value of 59%. The total doublet Gamow-Teller strength is determined much more precisely than the two individual contributions, because of a large negative correlation between the two parameters, $B_{a,GT}$ and $B_{b,GT}$. The total Gamow-Teller strength is constant within the errors to the value found in model 1.

4.4.3 Model 3

As a natural continuation of models 1 and 2, model 3 includes a narrow background level at 37 MeV with a width of 1.5 MeV. The fit is shown in Fig. 4.6.

Again the Gamow-Teller strength of the background level is increased, which is expected due to the same reason as in model 2. The positions of the 2^+ doublet levels are moved up towards the adopted values, and are now in good agreement with those found in Section 3.7.2. The width of the 16.9 MeV level is almost unchanged from model 2, while the width of the 16.6 MeV level is equal to the adopted value within the errors. The two mixing coefficients deviate with 5% of each other, but is showing better internal consistency than the previous models. The total doublet Gamow-Teller Strength is approximately unchanged from model 2.

The individual contributions show that they describe the doublet levels very well. In this model, the background level mostly contributes at lower energies. This also why the doublet parameters are in such good agreement with the two-level fit from Section 3.7.2. This model is therefore able to describe the spectrum very well, with nearly no change in the physical doublet levels.

4.4.4 Model 4

In the previous three models a background level with fixed energy at 37 MeV was chosen. This was done to test the results obtained in [Hyl10], but is not believed to be represent a physical level. In this model we let the background level parameters be based on physical known levels in the ^{8}Be spectrum. There are only three levels above 17 MeV known to decay by $\alpha - \alpha$ breakup, that couples to the 2^+ ground state in ^{8}B through allowed β-decay to their low energy tail. These are all $2^+ : 0$ levels, and the first two lies at 20.1 MeV, 22.2 MeV with widths of (880 ± 2) keV, ≈ 800 keV respectively. The last level lies at 25.2 MeV and the width is not know. To model the contributions from these levels, a background level is introduced at 22.0 MeV with a width of 900 MeV. The resulting fit is shown in Fig. 4.7, and the parameters are shown in Table 4.2.

The doublet energies in this model are 10 keV larger than those obtained in model 3, and are in agreement with the literature values within the errors. However, as the fit in Section 3.7.2 suggests an error in the determination of the excitation energy, this is most likely just a coincidence. This is further supported by the fact, that the β strength parameters are not correct. Also, in this model Γ_b is much smaller than any of the previous fits. These observations and the increased χ^2/dof suggests that this model does not give a clear description of the doublet levels. If the non-doublet contributions were due to higher-lying physical levels, this model should give a clear description of the physical doublet levels. This simple check is not enough to conclude anything, but model 4 does not suggest that the non-doublet contributions are solely due to higher-lying physical 2^+ levels.

Parameter	Model 1	Model 2	Model 3	Model 4
r_0 (fm)	1.35	1.35	1.35	1.35
$M_{a+b,GT}$	1.75(2)	1.71(3)	1.72(3)	1.80(3)
E_a (MeV)	16.499(3)	16.596(2)	16.615(2)	16625(2)
Γ_a (keV)	632(16)	132(2)	110(2)	116(2)
$B_{a,F}$	0.63(29)†	0.82(37)†	0.85(43)†	0.26(23)†
$B_{a,GT}$	1.45(17)	1.24(23)	1.19(26)	1.84(17)
E_b (MeV)	16.864(5)	16.898(4)	16.907(4)	16918(4)
Γ_b (keV)	145(13)	67(6)	65(6)	45(6)
$B_{b,F}$	1.37†	1.18†	1.15†	1.74†
$B_{b,GT}$	0.45(20)	0.59(24)	0.64(25)	0.17(18)
E_B (MeV)	37.0*	37.0*	37.0*	22.0*
Γ_B (MeV)	126*	24.0*	1.50*	0.90*
$B_{B,GT}$	0.0061(9)	0.14(1)	2.35(10)	0.70(4)
α_Γ^2	81%	66%	63%	72%
$\alpha_{B_F}^2$	69%	59%	58%	87%
$\chi^2/dof.$	1.05	1.04	1.04	1.06

Table 4.2: Fit parameters from R-matrix fits. All levels are 2^+ and the labeling is the following: a and b are the doublet levels and B is the background level. The mixing coefficient α_Γ is calculated using the doublet widths and Eq. (4.12), while α_{B_F} is calculated using Eq. (4.17). Parameters indicated with a * are fixed in the fit, and parameters with a † are fixed with respect to each other so they sum to 2.

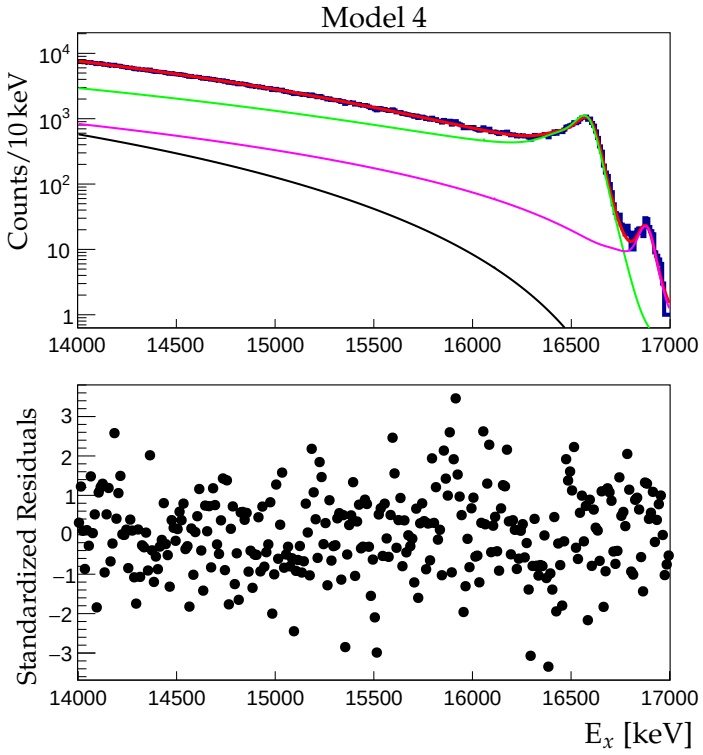

Figure 4.7: R-matrix fit of model 4 to data from IS633 above 14 MeV. The green, purple and thin blue lines are the contributions from the 16.6 MeV, 16.9 MeV and 22 MeV levels respectively. The thick blue line is the data and the red is the total R-matrix fit.

4.4.5 Discussion

Models 1, 2 and 3 are based on the background level used in model 2 in [Hyl10] and Section 4.3. These are used to examine the doublet levels' dependency on the width of the background level. The analysis shows, that the form of the background level has a large impact on the doublet level parameters. When comparing three models visually, we see that the individual contributions describe the doublet levels better, when using a narrow background level. In Model 1 the individual contributions do not describe the peak structure at all. In model 2, the individual contributions describe the peaks better, but the 16.6 MeV level is still lower than the visual peak. In model 3, the doublet levels are described very well by the individual contributions.

The fit to model 4 is an attempt to model physical levels in ^{8}Be. The background level is narrower than the one in model 3, but it also at lower energy only 5 MeV from the doublet. The resulting fit is a bit worse quality than those in

models 1-3, and the β strength parameters are almost purely placed in one level, suggesting a small mixing coefficient. This is not consistent with the widths obtained in the level. It is therefore not believed that the background contributions near the 2^+ doublet is due to higher-lying physical levels.

The two-level fit in Section 3.7.2 showed that a background contribution is needed, as evident by the bad fit quality. A good fit can be achieved with many different models, but this analysis shows that a narrow background level is well suited to describe the background, without changing the physical doublet parameters much. R-Matrix fits with background level widths down to 10 keV has also been made. All doublet parameters in these fits are in excellent agreement with those in model 3, and are therefore left out. The agreement is due to the fact that far away from the level when $(E - E_B)^2 \gg \Gamma_B^2/4$, the exact width of the level does not change the shape of the level much. A similar convergence is expected when broadening the level, but was not seen.

It it shown in Section 3.4.2 in [Hyl10], that it is possible to convert the doublet fit parameters into physical level parameters, even when using a broad background level. This is done using the transformation discussed in Section 4.1.2. However, a model that produces close to physical levels, is an advantage when determining the real doublet parameters, because it reduces errors associated with the parameter transformation. We can therefore say, that a narrow background level 37 MeV is very likely to be a good candidate for obtaining precise doublet parameters.

The total Gamow-Teller β strength is almost constant in all three models, which seems to indicate that it is not as model dependent as some of the other level parameters. The beta strength parameters converge towards more evenly distributed values between the doublet levels, for a narrow background. This corresponds to larger isospin mixing. For internal consistency in the fit, the mixing coefficient calculated from the Fermi strength parameters and the widths should be equal. This is not the case in any of the three models, as the mixing coefficient based in widths is constantly larger. The difference in mixing coefficients may indicate that the parametrization used (Eq. (4.8)) is not optimal. Mathematically there is no difference between the two β-decay types in Eq. (4.8). The only way they differ, is due to the interference with the background level. This may not be enough to differentiate between them, which is partially confirmed by the large correlations between $B_{a,F}$, $B_{a,GT}$ and $B_{b,GT}$[2]. The correlations lead to large uncertainties on the individual values but a well determined total Gamow-Teller strength.

An way to reduce these correlations, is to use Eqs. (4.16) and (4.17) in Eq. (4.8), to express the strengths in terms of mixing parameters and total Gamow-Teller

[2] $B_{b,F}$ is fixed with respect to $B_{a,F}$

strength. As one of the goals with this analysis is to measure the total doublet Gamow-Teller strength, this would likely give a more definitive answer. Also, to reduce the number of free parameters, one could use the mixing coefficients from the widths to force the aforementioned internal consistency. This re-parametrization has been attempted, but technical difficulties in ORM and lack of time prevented it from succeeding.

4.5 Summary

In this chapter we have introduced the theoretical framework R-matrix theory, used to describe nuclear resonances. This theory was used to analyze the extracted excitation energy spectrum for ^{8}Be, populated through β-delayed α-decay. Previous studies have shown that the three commonly known 2^+ levels are not enough to explain the strength of the spectrum, which led to the proposal of an intruder state in 1969. It is now most widely recognized, that the extra contributions are instead non-resonant and due to direct decay to the continuum.

The spectrum extracted in this study, is used to compare the results found in [Hyl10; Kir+11]. It is found that the model using a broad background level at 37 MeV, does not reproduce doublet levels that we believe are physical. There are two primary reasons for this conclusion. The first is that the individual doublet level contributions do not show a regular peak structure. Secondly, the 16.9 MeV shows signs of acting like a secondary background level. This is not visible in the JYFL08 spectrum, because there were no measured events belonging to this level. However, in the IS633 spectrum the R-matrix fit is seen to not be well centered around the 16.9 MeV peak. This, together with the bad fit quality suggests that the model is not able to describe the spectrum well.

Next, the doublet levels were analyzed using models with no 3 MeV level, and with varying background level parameters. Four different models were treated in this analysis. In the first three, the width of the background level was varied, while keeping the channel radius and energy constant. This led to the observation that when using a narrow background level, the doublet parameters converged towards the values found in the two-level fit from Section 3.7.2. This indicates that a narrow background level is able to describe the non-doublet contributions very well, and that the obtained doublet levels can be treated as almost pure physical levels.

Lastly, the 2^+ doublet levels were examined using a background level representing contributions from higher-lying known 2^+ states. The β strength parameters in this model were internally inconsistent and lead us to believe that the non-resonant contributions in the doublet region are not primarily due to higher-lying physical 2^+ states.

Chapter 5

Conclusion and Outlook

Using coincidence detections of the β-delayed $\alpha - \alpha$ breakup of ^{8}B, we have measured the ^{8}Be excitation spectrum. The primary aim of this analysis was to measure the level at 16.922 MeV, which is part of the isospin mixed 2^+ doublet at 16 MeV in ^{8}Be. Previously, only five counts of this level has been measured, which happened in 2008. In the spectrum from the present study, a clear and well-defined peak is seen, approximately centered around E_x =16.9 MeV. We have measured 284 coincidence events belonging to this peak, which is an improvement by a factor of 57. The estimated energy uncertainty of the spectrum at the 2^+ doublet is 11 keV. We also see indications that the spectrum is systematically lower at excitation energies around the 2^+ doublet. Trigger levels for the detectors limit the analyzed spectrum to excitation energies above 6 MeV, which prevents analysis of the broad 2^+ level at 3 MeV.

Two interfering Breit-Wigner levels have been fitted to data from both 2^+ doublet levels, providing peak positions and widths when neglecting contributions from other levels. Also, a two-level R-matrix fit was made, showing consistency with the Breit-Wigner fit. The two-level fit in Section 3.7.2 suggests, that the there may still be significant systematic errors in the E_x spectrum. This makes it difficult, if not impossible, to obtain reliable level parameters for the 2^+ doublet. There are two main concerns regarding the spectrum:

The first is concerned with the systematic error in the calibration. This could be improved by using a more sophisticated fitting algorithm. The AUSAlib Calibrator has the option to include secondary peaks in the calibration. This would add more data points in the linear calibration fit, and thereby maybe improve the calibration. However, as showed in Section 3.7.2, such an error can

not explain the full systematic error in the spectrum.

The second concern is the data reduction algorithm. The analysis in Sections 3.3 and 3.4 shows that the spectrum may include a significant number of false coincidences. It would be beneficial to conduct further analyses in order to either validate or improve the spectrum. Suggestions for this would be to make stricter conditions on the coincidence events. In particular, one could examine the energy dependency of the coincidence efficiency on events where particles hit the outermost pixels. Furthermore, another way to improve confidence in the line shape, is to add constraints on the positron. This would allow for an even more detailed kinematic analysis and a spectrum based on triple coincidences with two αs and a positron. However, this constraint will decrease the statistics significantly, and add a new layer of complexity to the analysis. Furthermore, the low energy positrons near the 2^+ doublet, are likely to be lost in the noise of the detectors.

In addition, a more detailed R-matrix analysis was conducted to compare the excitation energy spectrum to previous measurements. It was found that a model including a broad background level at 37 MeV results in an unphysical description of the 2^+ doublet. Variations of this model were tested in a fit using only part of the spectrum close to the doublet and neglecting the contribution from the 3 MeV level. This showed that a narrow background level at 37 MeV is better suited to describe effects not belonging to the doublet, in the region around the doublet. This results in a more direct description of the doublet levels.

Regarding the R-matrix analysis, we have barely scratched the surface in this study. The inability to fit to excitation energies below 6 MeV presents a severe problem for fitting the entire spectrum, because it is so heavily dominated by the contributions at 3 MeV. A way to circumvent this, is to use existing data together with the new spectrum, as in Section 4.3. If one were to investigate possible minute differences in the 2^+ spectrum from different probing mechanisms, an extremely precise determination of the entire spectrum would be needed. The intermediate region between the doublet and the 3 MeV level is especially crucial, as the background level is seen to have the largest relative contribution there. The greatest challenge with combining different datasets, is therefore to ensure a precise energy scale and normalization for the datasets, such that they are in perfect agreement. In addition to what was shown in Section 4.3, a comparison could be made on the 16.626 MeV level, to check for differences in the peak position.

The R-matrix analysis on the doublet levels showed extremely large correlations on the β strength parameters, which leads to a large uncertainty in the determination of the parameters. A way to improve this, is to change the

parametrization of Eq. (4.8) as suggested in Section 4.4.5. The hope is that such a re-parametrization would decrease the correlations in the β strength parameters, which would improve the determination of the precise total β strength for the doublet levels.

Bibliography

[BA02] M. Bhattacharya and E. G. Adelberger. "Reanalysis of α+α scattering and the β-delayed α spectra from ^{8}Li and ^{8}B decays". In: *Phys. Rev. C* 65 (5 May 2002), p. 055502.

[Bar00] R. Barlow. *SLUO Lectures on Statistics and Numerical Methods in HEP, Lecture 7: Fitting Method*. Aug. 2000.

[Bar68] F.C. Barker. "0^+ states of ^{8}Be". In: *Australian Journal of Physics* 21 (1968), p. 239.

[Bar69] F.C. Barker. "2^+ states of ^{8}Be". In: *Australian Journal of Physics* 22 (1969), pp. 293–316.

[BAS06a] M. Bhattacharya, E. G. Adelberger, and H. E. Swanson. "Precise study of the final-state continua in ^{8}Li and ^{8}B decays". In: *Phys. Rev. C* 73 (5 May 2006), p. 055802.

[BAS06b] M. Bhattacharya, E. G. Adelberger, and H. E. Swanson. "Precise study of the final-state continua in ^{8}Li and ^{8}B decays". In: *Phys. Rev. C* 73 (5 May 2006), p. 055802.

[BB08] B. Blank and M.J.G. Borge. "Nuclear structure at the proton drip line: Advances with nuclear decay studies". In: *Progress in Particle and Nuclear Physics* 60.2 (2008), pp. 403–483. ISSN: 0146-6410.

[BNQ13] S. Baroni, P. Navrátil, and S. Quaglioni. "Unified ab initio approach to bound and unbound states: No-core shell model with continuum and its application to ^{7}He". In: *Phys. Rev. C* 87 (3 Mar. 2013), p. 034326.

[Bre96] P. Brentano. "On the mixing of two bound and unbound levels: Energy repulsion and width attraction". In: *Physics Reports* 264 (1996), pp. 57–66.

[Bru02] C. R. Brune. "Alternative parametrization of R-matrix theory". In: *Phys. Rev. C* 66 (4 Oct. 2002), p. 044611.

[CER16] CERN. *ROOT*. 2016. URL: https://root.cern.ch/.

[Fay+98] M. S. Fayache et al. "Question of low-lying intruder states in ^{8}Be and neighboring nuclei". In: *Phys. Rev. C* 57 (5 May 1998), pp. 2351–2358.

[Hal18] J. Halkjær. *Energy Loss Calculator*. 2018. URL: https://eloss.phys.au.dk/.

[Hin+78] F. Hinterberger et al. "The alpha-alpha $\rightarrow$ 8Be double resonance at the 16.6 and 16.9 MeV levels". In: *Nuclear Physics A* 299.3 (1978), pp. 397–411. ISSN: 0375-9474.

[Hyl10] S. Hyldegaard. "Beta-decay studies of ^{8}B and ^{12}C". PhD thesis. Aarhus University, Department of Physics and Astronomy, Aug. 2010.

[ICR93] ICRU. "Stopping Powers and Ranges for Protons and Alpha Particles". In: *Report No. 49*. International Commission on Radiation Units and Measurements, 1993.

[Jon04] B Jonson. "Light dripline nuclei". In: *Physics Reports* 389 (Apr. 2004), pp. 1–59.

[JR75] F. James and M. Roos. "Minuit - a system for function minimization and analysis of the parameter errors and correlations". In: *Computer Physics Communications* 10.6 (1975), pp. 343–367. ISSN: 0010-4655.

[JW52] Blatt J.M. and V.F. Weisskopf. *Theoretical Nuclear Physics*. John Wiley and Sons, 1952.

[Kir+11] O. S. Kirsebom et al. "Precise and accurate determination of the ^{8}B decay spectrum". In: *Phys. Rev. C* 83 (6 June 2011), p. 065802.

[Kir10] O.S. Kirsebom. "^{8}B Neutrinos and ^{12}C Resonances". PhD thesis. Aarhus University, Department of Physics and Astronomy, Aug. 2010.

[Kol15] G.T. Koldste. "Deciphering drip-line decays - the case of ^{31}Ar". PhD thesis. Aarhus University, Department of Physics and Astronomy, Sept. 2015.

[Lab17] Brookhaven National Laboratory. *National Nuclear Data Center*. 2017. URL: https://www.nndc.bnl.gov/.

[LT58] A. M. Lane and R. G. Thomas. "R-Matrix Theory of Nuclear Reactions". In: *Rev. Mod. Phys.* 30 (2 Apr. 1958), pp. 257–353.

[MHK17] M. Munch, J. Halkjær, and O.S. Kirsebom. *AUSALIB - Aarhus Subatomic Library*. 2017. URL: `https://git.kern.phys.au.dk/ausa/ausalib/wikis/home`.

[MKR18] Michael Munch, Oliver Sølund Kirsebom, and Jonas Refsgaard. *Open R-matrix*. Feb. 2018. URL: `https://doi.org/10.5281/zenodo.1174079`.

[Pag05] Philip R. Page. "New broad ^{8}Be nuclear resonances". In: *Phys. Rev. C* 72 (5 Nov. 2005), p. 054312.

[PVG86] P.B. Pal, V.P. Varshney, and D.K. Gupta. "Total stopping power formulae for high energy electrons and positrons". In: *Nuclear Instruments and Methods in Physics Research Section B: Beam Interactions with Materials and Atoms* 16.1 (1986), pp. 1–4. ISSN: 0168-583X.

[Rii+15] K. Riisager et al. "Broad resonances and beta-decay". In: *Nuclear Physics A* 940 (Apr. 2015).

[Sig06] P Sigmund. *Particle Penetration and Radiation Effects*. Springer, 2006.

[Sme+99] M.H. Smedberg et al. "New results on the halo structure of 8B". In: *Physics Letters B* 452.1 (1999), pp. 1–7. ISSN: 0370-2693.

[TH10] I.S. Towner and J.C. Hardy. "The evaluation of V ud and its impact on the unitarity of the Cabibbo–Kobayashi–Maskawa quark-mixing matrix". In: *Reports on Progress in Physics* 73.4 (2010), p. 046301.

[Til+04] D.R. Tilley et al. "Energy levels of light nuclei A=8,9,10". In: *Nuclear Physics A* 745.3 (2004), pp. 155–362. ISSN: 0375-9474.

[Vog04] Erich Vogt. "R-Matrix Theory". In: *Lecture notes for the R-Matrix School of the Joint Institute for Nuclear Astrophysics at Notre Dame University*. South Bend Indiana, Oct. 2004.

[Vog62] Erich Vogt. "Theory of Low Energy Nuclear Reactions". In: *Rev. Mod. Phys.* 34 (4 Oct. 1962), pp. 723–747.

[War86a] E. K. Warburton. "R-matrix analysis of the $\beta^{\mp}$-delayed alpha spectra from the decay of ^{8}Li and ^{8}B". In: *Phys. Rev. C* 33 (1 Jan. 1986), pp. 303–313.

[War86b] E. K. Warburton. "R-matrix analysis of the $\beta^{\mp}$-delayed alpha spectra from the decay of ^{8}Li and ^{8}B". In: *Phys. Rev. C* 33 (1 Jan. 1986), pp. 303–313.

[Wir+06] W.T. Wiringa et al. "The ^{8}B neutrino spectrum". In: *Phys. Rev. C* 73 (2 Feb. 2006).

[Wir+13] R. B. Wiringa et al. "Charge-symmetry breaking forces and isospin mixing in ^{8}Be". In: *Phys. Rev. C* 88 (4 Oct. 2013), p. 044333.

[WM74] D.H. Wilkinson and B.E.F. Macefield. "A parametrization of the phase space factor for allowed β-decay". In: *Nuclear Physics A* 232.1 (1974), pp. 58–92. ISSN: 0375-9474.

[Zie18] J.F. Ziegler. *SRIM - The Stopping and Range of Ions in Matter*. 2018. URL: http://www.srim.org/.

[ZZB10] J.F. Ziegler, M.D. Ziegler, and J.P. Biersack. "SRIM – The stopping and range of ions in matter (2010)". In: *Nuclear Instruments and Methods in Physics Research Section B: Beam Interactions with Materials and Atoms* 268.11 (2010). 19th International Conference on Ion Beam Analysis, pp. 1818–1823. ISSN: 0168-583X.

[ZZB15] J.F. Ziegler, M.D. Ziegler, and J.P. Biersack. *SRIM - The Stopping and Range of Ions in Matter*. 15th. (n.p.), 2015.